

Cascade of transitions in twisted and non-twisted graphene layers within the van Hove scenario

Dmitry V. Chichinadze,¹ Laura Classen,² Yuxuan Wang,³ and Andrey V. Chubukov^{1,4}

¹*School of Physics and Astronomy, University of Minnesota, Minneapolis, MN 55455, USA**

²*Max Planck Institute for Solid State Research, D-70569 Stuttgart, Germany*

³*Department of Physics, University of Florida, Gainesville, Florida 32601*

⁴*W. I. Fine Theoretical Physics Institute,*

University of Minnesota, Minneapolis, Minnesota 55455, USA[†]

Abstract

Motivated by measurements of compressibility and STM spectra in twisted bilayer graphene, we analyze the pattern of symmetry breaking for itinerant fermions near a van Hove singularity. Making use of an approximate SU(4) symmetry of the Landau functional, we show that the structure of the spin/isospin order parameter changes with increasing filling via a cascade of transitions. We compute the feedback from different spin/isospin orders on fermions and argue that each order splits the initially 4-fold degenerate van Hove peak in a particular fashion, consistent with the STM data and compressibility measurements, providing a unified interpretation of the cascade of transitions in twisted bilayer graphene. Our results follow from a generic analysis of an SU(4)-symmetric Landau functional and are valid beyond a specific underlying fermionic model. We argue that an analogous van Hove scenario explains the cascade of phase transitions in non-twisted Bernal bilayer and rhombohedral trilayer graphene.

INTRODUCTION

Twisted bilayer graphene (TBG) is a two-dimensional correlated electronic system, which exhibits superconductivity [1–3] and correlated phases [4–13]. The focus of our work is the analysis of a cascade of phase transitions near integer fillings $|n| = 1, 2, 3, 4$, detected in STM and electronic compressibility measurements [5, 14, 15] (panels (a)-(e) in Fig. 1). Compressibility measurements show sharp seesaw features of $d\mu/dn$ near integer $|n|$, and STM data show that around each of these n a peak in the density of states splits, and one of its components appears on the other side of the Fermi level. For the interpretation, the authors of [14] adopted a strong coupling approach and associated the observed STM peaks with narrow sub-bands. They argued that at each transition one sub-band crosses the Fermi level, moves away from it, and becomes incoherent. The authors of [15] interpreted compressibility data within a moderate coupling scenario of a 4-fold spin/isospin degenerate band and argued that the cascade can be understood as a series of interaction-driven transitions. They conjectured that at, e.g., electronic doping one of the bands gets completely filled at each transition, while the occupation of the remaining ones gets depleted; mirror symmetric behavior holds for hole doping.

In this communication we propose the scenario in which the cascade of transitions is caused by the

* chich013@umn.edu

† achubuko@umn.edu

development of particle-hole orders, like in [15], but we specifically identify the STM peaks with van Hove (vH) singularities. We argue that the components of the initially 4-fold degenerate vH peak move through the Fermi level one by one, but remain close to it. The split peaks recombine into a single 4-fold peak at $|n| \lesssim 4$, when electronic order vanishes. Our scenario is illustrated in panels (a), (c), and (f) in Fig. 1.

A cascade of transitions has been observed near van Hove doping in less correlated non-twisted Bernal bilayer (BBG) and rhombohedral trilayer graphene (RTG) [16–19]. We show that our vH scenario equally explains the sequence of transitions in these materials. We believe that the similarity between the ordered states and electronic reconstruction in BBG/RTG and in TBG supports a moderate coupling vH-based approach. We emphasize, however, that we use this approach specifically to describe the cascade of phase transitions with doping. A strong coupling approach is needed for explaining the insulating behavior of TBG near integer fillings.

We further emphasize that (i) vH peaks have been observed in TBG at different twisting angles [6, 20], (ii) are present in the electronic dispersion, obtained in first-principle calculations, and in the one renormalized by the interaction, even if the bottom of the dispersion moves away from Dirac points [21], and (iii) the cascade of transitions, observed in magic-angle twisted trilayer graphene, has been argued to be triggered by vH peaks, at least at high displacement fields [22]. The vH scenario has been also discussed in context of chiral density wave and superconductivity in TBG (see e.g., [23–27]).

The summary of our results for TBG is presented in Fig. 1 along with the experimental data from Refs. [14, 15]. We label the vH peaks in conduction (valence) bands in by I (II) and label peak components by a,b,c,d. Our interpretation of the STM data from Ref. [14] for electron doping (panel (b)) is the following: as the system moves away from charge neutrality, the 4-fold degenerate peak $I_{a+b+c+d}$ approaches μ from above, and at $n \leq 1$, splits in a 3-1 fashion: three components I_{a+b+c} stay above μ , and one component, I_d , jumps to below the Fermi level, but remains close to it. At $n \leq 2$, the three components again come close to μ , and the vH peak I_{a+b+c} splits in 2-2 fashion, such that I_{a+b} moves back, while I_c jumps to below the Fermi level and merges with I_d into I_{c+d} . At $n \lesssim 3$, I_{a+b} splits and I_b jumps to below the Fermi level and merges with I_{c+d} into I_{b+c+d} . Finally, at $n \lesssim 4$, the last component I_a jumps across the Fermi level and merges with three other components into 4-fold degenerate $I_{a+b+c+d}$. For hole doping the overall evolution is the same, but the data seem to show a more gradual behavior: the components of peak II in panel (d) cross the Fermi level one-by-one, indicating

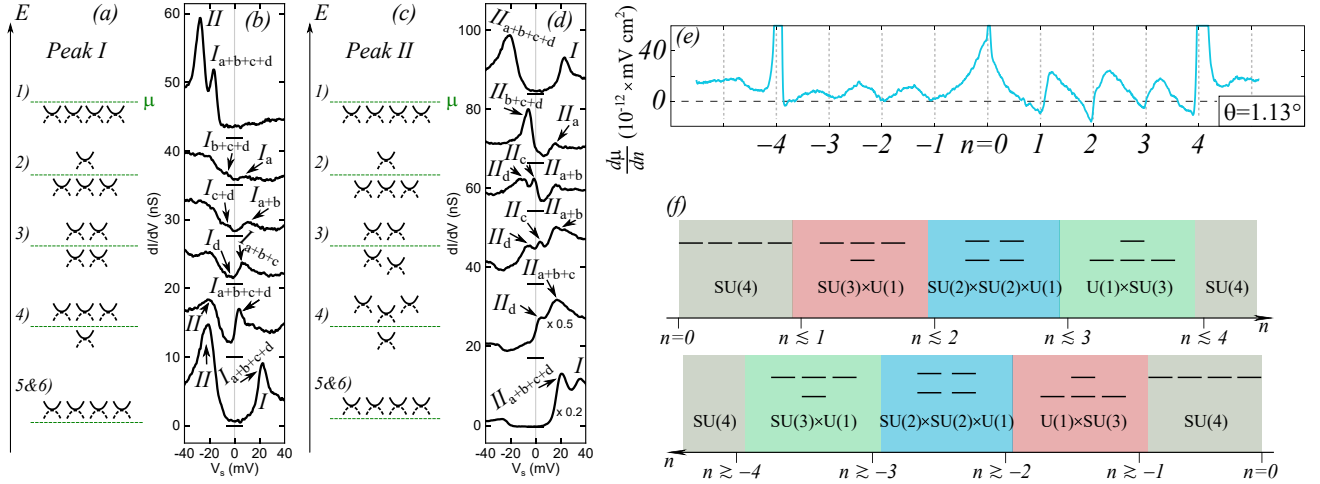


FIG. 1. The cascade of electronic transitions in twisted bilayer graphene. (a)–(d): the proposed splitting of the initially 4-fold (spin and valley) degenerate vH peak upon raising the electron filling n (panels (a), (b)) and hole filling (panels (c), (d)), and the corresponding STM data for twist angle of 1.06° , reproduced with permission from the authors of Ref. [14]. The van Hove peaks in the conduction (valence) bands are labeled by I (II), and subscripts a,b,c,d label the 4 peak components. (e): experimental data for inverse compressibility with seesaw features, interpreted as a cascade of phase transitions. Reproduced with permission from the authors of Ref. [15]. The data are for twist angle $\theta = 1.13^\circ$, (f) The schematic phase diagram of TBG upon electron or hole doping, based on comparison between the theory and the STM data. Within our model, we obtained $SU(3) \times U(1)$ ($U(1) \times SU(3)$) symmetry for both electron and hole doping at $1 < |n| < 2$ ($3 < |n| < 4$), corresponding to 3-1 (1-3) splitting, but it is reduced to $SU(2) \times U(1) \times U(1)$ ($U(1) \times U(1) \times SU(2)$) if there is an intermediate phase with 2-1-1 (1-1-2) splitting, as STM data for hole doping likely indicate.

the presence of an intermediate state between 3 – 1 and 1 – 3 ones.

We consider these data as evidence that once the 4-fold degenerate vH peak gets close to μ at $|n| \sim 1$ (peak I for $n > 0$ and peak II for $n < 0$), the system develops a vH-induced particle-hole order. The order exists between $|n| \lesssim 1$ and $|n| \lesssim 4$ and reconstructs the fermionic spectra, pushing vH peaks in some bands above μ and in other band(s) below μ . The structure of the order changes near $|n| = 2$ and $|n| = 3$, via first-order transitions, and this changes the splitting of the vH peak and simultaneously gives rise to sharp changes in the compressibility (see Fig. 1 (e)).

Here, we present the theoretical description of this scenario within the model of interacting itinerant electrons whose band structure has a vH singularity near μ . We use as an input our earlier result [28, 29]

that the increased density of states near the vH singularity enables a spontaneous symmetry breaking in spin and valley spaces (for particle-hole orders with zero transferred momentum electronic DOS has to exceed a threshold in order to satisfy the Stoner-type criterion). For a model with intra-site (Hubbard) and assisted hopping interactions within a given hexagon [30], we found 15 particle-hole order parameters, for which the couplings are attractive, near-equal, and larger than for other order parameters. They describe intra-valley order at zero momentum ($\mathbf{Q} = 0$) and inter-valley density waves ($\mathbf{Q} \neq 0$). These 15 order parameters are described by 4×4 matrices in spin and valley spaces, specified by spin σ and valley isospin τ and form the adjoint representation of the SU(4) group. For shortness, we call an order in (σ, τ) space a spin/isospin order. An SU(4)-symmetric order parameter manifold and the interplay between spin and isospin orders have been recently discussed in [30–37] – these works provide additional motivation for us. Another input for our analysis are band structure calculations [38, 39], which reported the pinning of the vH singularity to the chemical potential over the range of n .

We derive and analyze the Landau free energy for an SU(4)-symmetric fermionic model. We argue that there are three sets of ordered states, which split the 4-fold degenerate vH peak in three different ways. The first vH-induced instability splits the vH peak in a 3-1 fashion, with peaks for 3 degenerate bands shifting towards charge neutrality, and the remaining peak moving to below μ . As the magnitude of a spin/isospin order increases, the system undergoes a transition into a different ordered state, which splits the vH peak into a 2-2 fashion. The transition is first-order in our model, but in reality may occur via an intermediate phase with 2-1-1 splitting. At $|n| \sim 3$ the magnitude of the order starts decreasing as some of vH peak components move further away from μ , and the system behavior goes in reverse - first the system undergoes a transition into an ordered state which gives rise to 1-3 vH peak splitting, again either via a direct first-order transition, or via an intermediate phase with 1-1-2 splitting, and then, at even larger $|n| \leq 4$, the order vanishes, and all 4 vH peak components merge into a single vH peak below μ .

We use the same approach for BBG and RTG. The bands structures and Fermi surfaces of BBG and RTG are very similar, and we model both systems by an effective patch model of fermions, located in the vicinity of \mathbf{K} and \mathbf{K}' points in the BZ. We find that the 15 leading instabilities are analogous to TBG: towards valley polarization and intra-valley spin order (both with $\mathbf{Q} = 0$) and towards inter-valley charge and spin density wave orders with $\mathbf{Q} = \mathbf{K} - \mathbf{K}'$. We find that for a Hubbard interaction,

these orders are described by the same SU(4)-symmetric Landau free energy functional, Eqs. (1) and (2), as in TBG. Like in TBG, the first vH-induced transition is into a state with valley polarization and ferromagnetism in a single valley. This order gives rise to $3 - 1$ splitting, which in the case of BBG/RTG gives rise to one larger and three smaller Fermi pockets. This splitting is analogous to the one observed in the IF_1 state in the notations of Ref. [16]. The subsequent transition upon doping is into a state with either pure valley charge order or ferromagnetic order in both valleys. This state gives rise to $2 - 2$ splitting, which in BBG/RTG gives rise to two larger and two smaller Fermi pockets. This is analogous to PIP_2 state [16]. A potential intermediate state with $2 - 1 - 1$ splitting is analogous to PIP_1 state in [16].

RESULTS

Cascade of transitions in TBG Band structure calculations show that there are eight bands within the flat-band regime of TBG, accounting for two spin projections, two valley degrees of freedom from the original graphene layers, and two sublattices of the moiré superlattice. Four bands are with upward and four with downward dispersion, merging at Dirac points \mathbf{K} and \mathbf{K}' . Upon electron (hole) doping the chemical potential moves up (down), simultaneously changing the filling of four bands. Each band displays a vH singularity. The vH singularities for four conduction (four valence) bands are at the same energy. It was argued that strong coupling renormalizations may shift the minimum of electron band to the Γ point [21, 38], but vH singularities remain even for the renormalized dispersion [38, 40].

We study the cascade of phase transitions by analyzing the Landau free energy for the ordered phases of fermions with vH singularity near μ . The order parameters are expectation values of fermionic bilinears, and the free energy can be obtained by departing from a microscopic model of vH fermions with 4-fermion Hubbard and assisted hopping interactions [30] and integrating out fermions after performing a Hubbard-Stratonovich transformation. Alternatively, one can write down the Landau free energy solely based on symmetries and fix parameters phenomenologically through comparison with experiments. In an earlier study [29] we found that out of a large number of possible fermionic bilinears (143 in the 6-patch vH model and even larger number in 12-patch model) there are 15, for which the couplings are attractive and the largest by magnitude. The set of 15 is composed of two subsets of 7 and 8 bilinears with a single coupling within each subset. 7 bilinears with coupling λ_7 are intra-valley with transferred momentum $\mathbf{Q} = 0$, and 8 with coupling λ_8 are inter-valley with a finite \mathbf{Q} (Kekule-type

states considered in [41]).

The couplings λ_7 and λ_8 are not identical, but are close to each other [28]. In our analysis we treat λ_7 and λ_8 as equal, in which case the 15 bilinears form an adjoint representation of SU(4). We checked that the cascade of transitions and the sequence of vH peak splitting is the same in the model with only 7 bilinears (the case $\lambda_7 > \lambda_8$). In the model with 8 bilinears there is a single ordered phase and no cascade.

For the SU(4) case, the Landau free energy up to fourth order is [29] [42]

$$\mathcal{F} = -\frac{\alpha}{2}\text{Tr}[\hat{\Phi}^2] + \frac{\gamma}{3}\text{Tr}[\hat{\Phi}^3] + \frac{\beta}{4}\text{Tr}[\hat{\Phi}^4] + \frac{\beta'}{4}\text{Tr}[\hat{\Phi}^2]^2, \quad (1)$$

where $\hat{\Phi} = \sum_{j=1}^{15} \phi_j T^j$, T^j are generators of SU(4), and $\phi_j \sim f^\dagger T^j f$ are fermionic bilinears, which we treat as Hubbard-Stratonovich fields (f and f^\dagger are operators of electrons near vH points). The term β' does not appear within Hubbard-Stratonovich but is allowed by symmetry, and we keep it for generality.

By construction, $\hat{\Phi}$ can be represented by a traceless matrix [43]. In the diagonal basis

$$\hat{\Phi} = \text{diag}(\lambda_1, \lambda_2, \lambda_3, -(\lambda_1 + \lambda_2 + \lambda_3)), \quad (2)$$

and the free energy is

$$\begin{aligned} \mathcal{F} = & -\frac{\alpha}{2} \left(\sum_j \lambda_j^2 + \left(\sum_j \lambda_j \right)^2 \right) + \frac{\gamma}{3} \left(\sum_j \lambda_j^3 - \left(\sum_j \lambda_j \right)^3 \right) \\ & + \frac{\beta}{4} \left(\sum_j \lambda_j^4 + \left(\sum_j \lambda_j \right)^4 \right) + \frac{\beta'}{4} \left(\sum_j \lambda_j^2 + \left(\sum_j \lambda_j \right)^2 \right)^2. \end{aligned} \quad (3)$$

At $\gamma = 0$, the order develops continuously when α changes sign and becomes positive. At a finite γ , the transition is necessarily first order and occurs already when α is negative. Below we restrict to $\alpha > 0$, when the order is already finite and also set $\beta > 0$, consistent with the Hubbard-Stratonovich analysis and the calculation of α, β for the tight-binding model near a vH singularity [29]. We discuss the behavior of γ below and in Supplementary Discussion V. Minimizing \mathcal{F} with respect to λ_j ($j = 1, 2, 3$), we find three solutions (up to permutations of λ_j): (i) $\lambda_1 = \lambda_2 = \lambda_3$; (ii) $\lambda_1 = \lambda_2 = -\lambda_3$; (iii) $\lambda_1 = \lambda_2 \neq \lambda_3$ (see Supplementary Discussion I for details). For the first solution, $\hat{\Phi} = \text{diag}(\lambda, \lambda, \lambda, -3\lambda)$, and the broken symmetry is described by the coset SU(4)/[SU(3)×U(1)], where SU(3) corresponds to the transformation within the subset of the first three components of $\hat{\Phi}$, and U(1) to a rotation of the last component relative to the other three. The ordered states in terms of expectation values of

fermionic bilinears $\langle \phi_i \rangle$ are mixtures of spin/isospin order with particular ratios of spin and isospin components [29]. For example, a pure intra-valley order is a part of this set, but a pure inter-valley order is not. The order parameter manifold has $15 - 8 - 1 = 6$ Goldstone modes. The feedback of this order on fermions is 3-1 or 1-3 splitting of vH peaks, depending on the sign of γ . For the second solution, $\hat{\Phi} = \text{diag}(\lambda, \lambda, -\lambda, -\lambda)$, and the broken symmetry is $\text{SU}(4)/[\text{SU}(2) \times \text{SU}(2) \times \text{U}(1)]$, where the two $\text{SU}(2)$'s correspond to rotations within the subsets of the first two and the last two components of $\hat{\Phi}$, and $\text{U}(1)$ corresponds to a rotation of one subset relative to the other. The ordered states in terms of $\langle \phi_i \rangle$ include pure spin and isospin orders, e.g. intra-valley ferromagnetism and valley polarization, and various inter-valley density waves [29]. This manifold has $15 - 6 - 1 = 8$ Goldstone modes. The feedback from such order on fermions leads to 2-2 splitting of the vH peaks. Finally, the third solution describes a mixed state with $\hat{\Phi} = \text{diag}(\lambda, \lambda, -\lambda_3, -2\lambda + \lambda_3)$ and broken symmetry $\text{SU}(4)/[\text{SU}(2) \times \text{U}(1) \times \text{U}(1)]$. The order parameter manifold contains $15 - 3 - 1 - 1 = 10$ Goldstone modes. The feedback on fermions leads to 2-1-1 or 1-1-2 splitting of vH peaks.

The values of λ and the free energies for the three states, $F_l = \frac{\alpha^2}{\beta} f_l(x, y)$, are functions of $x = \gamma / \sqrt{\alpha\beta}$ and $y = \beta' / \beta$:

$$\begin{aligned}
(i) \lambda_i &= \sqrt{\frac{\alpha}{\beta}} \frac{|x| \pm \sqrt{x^2 + 7 + 12y}}{7 + 12y}, \quad f_i(x, y) = -\frac{(|x| \pm \sqrt{7 + x^2 + 12y})^2 [3(7 + 12y) + 2|x|(|x| \pm \sqrt{7 + x^2 + 12y})]}{(7 + 12y)^3} \\
(ii) \lambda_{ii} &= \sqrt{\frac{\alpha}{\beta}} \frac{1}{\sqrt{1 + 4y}}, \quad f_{ii}(x, y) = -\frac{1}{1 + 4y} \\
(iii) \lambda_{iii} &= \sqrt{\frac{\alpha}{\beta}} x, \quad \lambda_{iii,3} = \sqrt{\frac{\alpha}{\beta}} \left(\sqrt{\frac{1 - x^2(1 + 4y)}{1 + 2y}} - |x| \right), \quad f_{iii}(x, y) = -\frac{1 + 2x^2 - x^4(1 + 4y)}{2(1 + 2y)}. \tag{4}
\end{aligned}$$

The solution (iii) exists for $|x| \leq 1 / \sqrt{1 + 4y}$ and the \pm sign is for positive/negative γ . We plot the free energy prefactors $f_l(x, y)$ in Fig. 2.

We see that at large $|x|$ the ground state configuration is state (i) while for small $|x|$ it is state (ii). There is a direct first-order transition between states (i) and (ii) at some intermediate $|x| = x_{\text{cr}}$. We expect that $\alpha > 0$ between $1 < |n| < 4$, where the vH peak remains near the chemical potential, and argue that γ changes sign from positive to negative as $|n|$ increases, because the sign of γ is different when the bands are empty and when they are filled. As a result x evolves from a large positive value to a large negative one via zero upon increasing $|n|$. Because small α corresponds to large $|x|$, when the order first emerges, the system moves into state (i), and the components of the vH peak split in

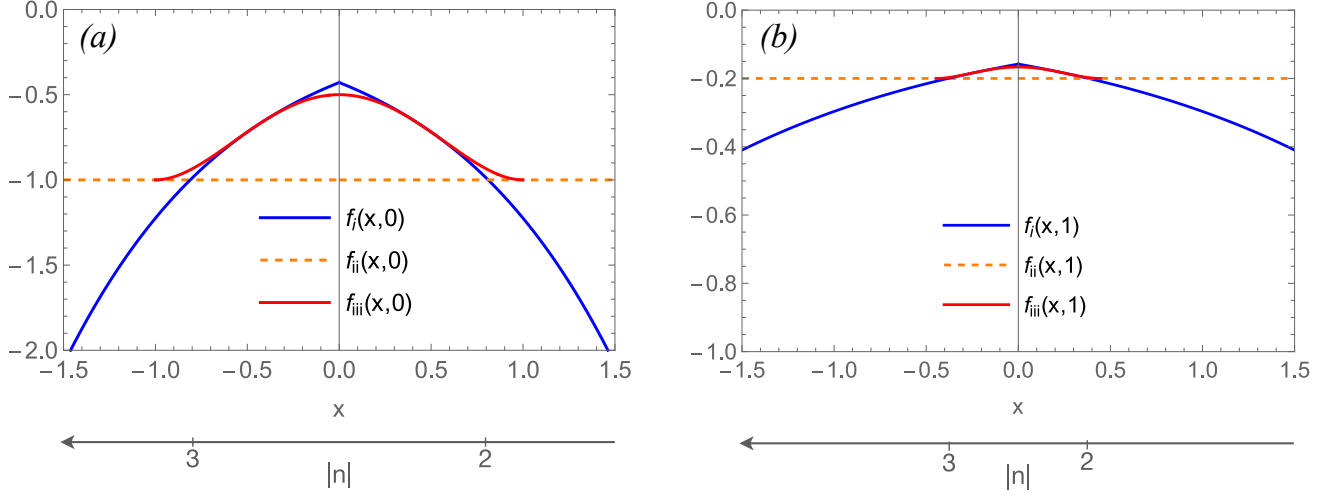


FIG. 2. **Landau free energy.** The functions $f_l(x, y)$ from Eq. (4), with $l = i, ii, iii$, shown as functions of $x = \gamma / \sqrt{\alpha\beta}$ for two values of $y = \beta' / \beta$: $y = 0$ (panel (a)) and $y = 1$ (panel (b)). The free energies are $F_l = (\alpha^2 / \beta) f_l(x, y)$, hence the smallest $f_l(x, y)$ determines the ground state. The states (i) and (ii) are the ones for which the vH peaks split in 3-1 (1-3) and 2-2 fashion, respectively. The state (iii) is an intermediate state with 2-1-1 (1-1-2) splitting. This intermediate state does not appear as a ground state in our model for all y , but its energy is close to those of (i) and (ii) near critical x of the first-order transition between the two, and it can potentially become a ground state around this x if we move away from $SU(4)$ -symmetric model by e.g., including interaction terms with inter-valley scattering. The relation between x and $|n|$ is shown at the bottom.

1-3 fashion for positive γ . As α increases, $|x|$ decreases and eventually reaches x_{cr} , where the system undergoes a first order transition into the ordered state (ii), for which the splitting of the components of the vH peak is 2-2. At larger n , γ changes sign and its magnitude increases, while α starts decreasing. As a result, $|x|$ increases. When it reaches x_{cr} , the system undergoes another first-order transition into the state, which gives rise to 3-1 splitting of the components of the vH peak. Eventually the order disappears and all 4 components of the vH peak recombine into a single peak. We also note that while the intermediate state (iii) is not the ground state for any x and y , its free energy F_{iii} is only slightly larger than F_i and F_{ii} at $|x|$ near x_{cr} . This is particularly so at large y (at $x_{cr} \approx \sqrt{3/16y}$, F_{iii} is larger than $F_i = F_{ii}$ by $(\alpha^2 / \beta) 1 / (16y)^2$). Thus, it seems possible that the intermediate state (iii) will become the ground state once we move away from an $SU(4)$ -symmetric model by e.g., including interaction terms

with inter-valley scattering. Such terms are small, but finite in TBG [30, 44, 45]. If the transition from (i) to (ii) is via the intermediate phase (iii), there is a range of $|n|$ where the splitting of the vH peak components is 2-1-1 or 1-1-2, again depending on the sign of γ . Some indications of 2-1-1 and 1-1-2 splitting have been found in STM for hole-doped samples [5, 14].

Cascade of transitions in BBG and RTG

The same analysis can be applied to study the cascade of phase transitions in BBG and RTG. In both systems, application of an electric field opens a gap between conduction and valence bands and flattens the fermionic dispersion near Dirac \mathbf{K} and \mathbf{K}' points [46]. Near charge neutrality, this creates small Fermi pockets, three near \mathbf{K} and three near \mathbf{K}' . Upon doping, pockets merge at vH fillings and eventually transform into one larger pocket near \mathbf{K} and one near \mathbf{K}' (Refs. [47–52]). We consider the full 6-pocket model in Supplementary Discussion XI and here illustrate the behavior using a simplified model of fermions in two patches near \mathbf{K} and \mathbf{K}' with Hubbard intra-patch and inter-patch density-density interaction. In this model, electronic instabilities towards valley polarization, intra-valley ferromagnetism, and inter-valley spin and charge order all occur at the same critical coupling λ . These 15 bilinears then form an adjoint representation of SU(4) and are described by the same Landau free energy functional as in (1). The cascade of transitions in BBG and RTG then matches the one in TBG with the only difference that some pockets may sink below the Fermi level (see Fig. 3). In a more realistic 6-patch model, the coupling for 7 C_3 symmetry preserving order parameters with $\mathbf{Q} = 0$ is not the same as for order parameters with momenta \mathbf{Q} close to $\mathbf{K} - \mathbf{K}'$. The sequence of transition and the Fermi surface reconstruction remain the same as in the 2-patch model if the order develops with $\mathbf{Q} = 0$.

Comparison with experiments on TBG In our proposed vH scenario, spin/isospin order develops at $|n| \lesssim 1$, when the four-fold degenerate vH peak approaches the Fermi level, and persists up to $|n| \lesssim 4$. In this range of n , the vH peak splits, but according to STM data, its components are still located near the Fermi energy, i.e., the enhancement of the DOS near the Fermi level persists. At larger $|n|$, the vH peak again becomes four-fold degenerate and moves away from the Fermi level. The evolution of spin/isospin order and of its feedback on the components of the vH peak is governed in our theory by the relative strength of the prefactor of the cubic term in the Landau free energy (specifically, by $x = \gamma / \sqrt{\alpha\beta}$). This prefactor is expressed via a convolution of three fermionic propagators and vanishes for particle-hole symmetry around the Fermi surface. In the absence of such symmetry, γ is non-zero. We conjecture that x is positive near $n = 1$ passes through zero at $2 < n < 3$, and becomes negative at

larger n (see Supplementary Discussion V for more discussion on this). We then end up with the phase diagram in Fig. 1 (f). There are two phase transitions between disordered and ordered states at $|n| \lesssim 1$, and $|n| \lesssim 4$, and two transitions between different ordered phases at $|n| \lesssim 2$ and $|n| \lesssim 3$. Specifically, within our theory the sequence for the symmetry-breaking pattern and the degeneracy of the vH peak is:

$$\begin{aligned}
n \lesssim 1: & \text{SU}(4) \rightarrow \text{SU}(3) \times \text{U}(1) : (4, 0) \rightarrow (3, 1) \\
n \lesssim 2: & \text{SU}(3) \times \text{U}(1) \rightarrow \text{SU}(2) \times \text{SU}(2) \times \text{U}(1) : (3, 1) \rightarrow (2, 2) \\
n \lesssim 3: & \text{SU}(2) \times \text{SU}(2) \times \text{U}(1) \rightarrow \text{U}(1) \times \text{SU}(3) : (2, 2) \rightarrow (1, 3) \\
n \lesssim 4: & \text{U}(1) \times \text{SU}(3) \rightarrow \text{SU}(4) : (1, 3) \rightarrow (0, 4)
\end{aligned} \tag{5}$$

where a and b in (a, b) indicate the number of vH peaks above and below μ for the case of electron doping. For hole doping the sequence is identical, except a and b in (a, b) are interchanged. If the transformations $(3, 1) \rightarrow (2, 2)$ and $(2, 2) \rightarrow (1, 3)$ occur via an intermediate phase (c), each of the two first-order transitions around $|n| = 2$ is replaced by two second-order transitions with the intermediate structure of vH peaks $(2, 1, 1)$ and $(1, 1, 2)$.

The theoretical phase diagram agrees with the STM results [5, 14] (Fig. 1 (b,d)) including fine details, lending support to our theory. Note, that there is no symmetry of the phase diagram with respect to $|n| = 2$, i.e. the transitions at $|n| \lesssim 1$ and $n \lesssim 3$ are different ones (there is an approximate symmetry with respect to $|n| = 2.5$). The theory also explains the seesaw behavior of electron compressibility, reported in [15] and shown in Fig. 1 (e). Our reasoning is the following. As doping increases and the system approaches one of transitions from the cascade, the inverse compressibility $d\mu/dn$ decreases as the n -times degenerate vH peak approaches the Fermi level, where $d\mu/dn = 0$ ($n = 4, 3, 2$, depending on the number of the transition in the cascade). After a new order develops, one peak component crosses the Fermi level, while the other $(n - 1)$ components move back from the Fermi level. Because all vH peaks move away from the Fermi level in a first-order transition, $d\mu/dn$ jumps to a larger value. As doping increases further towards the next transition from the cascade, the $(n - 1)$ - times degenerate vH peak approaches the Fermi level, and $d\mu/dn$ again decreases towards zero. Then the new order develops, one peak component crosses the Fermi level, while the other $(n - 2)$ components move back from it, and $d\mu/dn$ again jumps to a higher value. This gives rise to seesaw structure of the inverse compressibility (see Supplementary Discussion V for an example calculation of $d\mu/dn$ for one

transition of the cascade). Because all four vH peak components remain close to the Fermi level, all four contribute to the evolution of $d\mu/dn$ between the transitions. This is consistent with a weak dependence of the slope of $d\mu/dn$ on the number of a transition in the cascade.

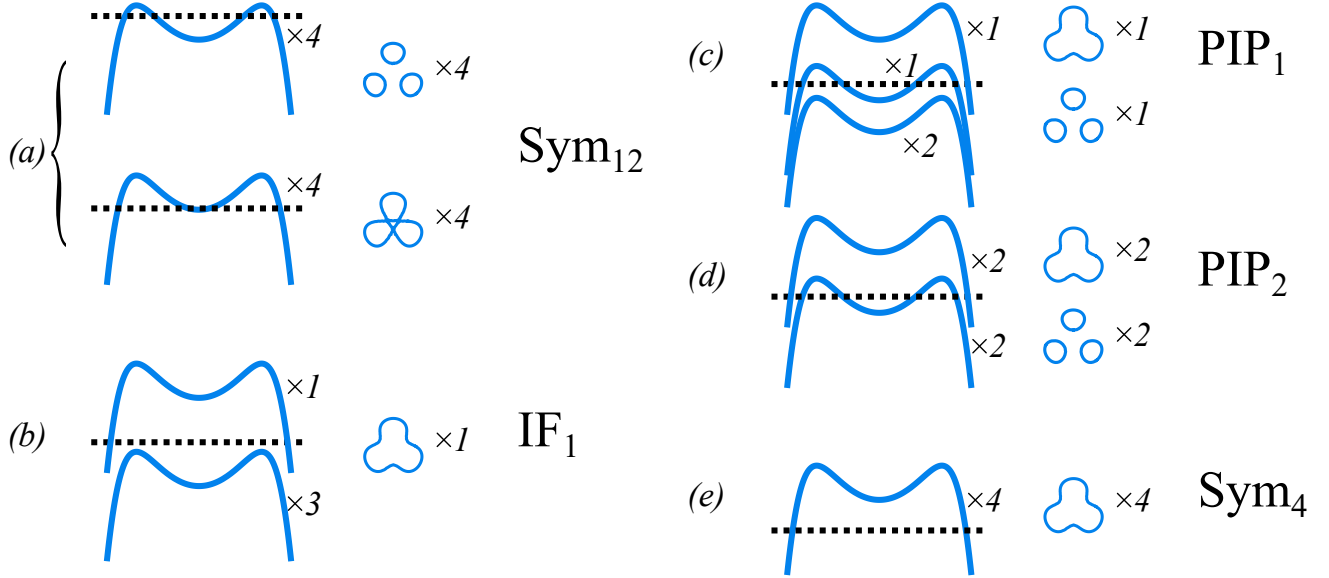


FIG. 3. **The cascade of transitions in BBG/RTG.** The notations – the same as in [16, 19], are as follows: IF₁ – isospin ferromagnet, PIP₁ – partially isospin-polarized phase with one large Fermi surface and one small, PIP₂ – partially isospin-polarized phase with two large Fermi surface and two small, Sym₄ – a symmetric phase with 4 identical large Fermi surfaces (one per isospin), Sym₁₂ – a symmetric phase with 12 identical small Fermi surfaces (three per isospin). The states in panels (a)-(e) are symmetric four-fold degenerate, 1 – 3, 1 – 1 – 2, 2 – 2, and again symmetric four-fold degenerate, correspondingly. The 3 – 1 and 2 – 1 – 1 states have not been detected in [16] and are not shown. The 3 – 1 and 2 – 1 – 1 states have not been detected in [16] and are not shown. The small pockets in 1 – 3 (IF₁) are assumed to sink below the Fermi level. The symmetry between three small pockets in panels (c) and (d) may be broken by subleading interactions, leaving only one small pocket, as the data in [16] indicate.

Comparison with experiments on BBG/RTG Measurements of inverse electronic compressibility and magnetoresistance in BBG [16, 17] and RTG [19] at a finite displacement field revealed a cascade of transitions upon hole or electron doping. The fermionic structure of the two materials is almost identical, and for definiteness we focus on hole-doped BBG. Near charge neutrality, the system is in the valley/spin symmetric state (labeled Sym₁₂ in Ref. [16] and in Fig. 3 (a)) with twelve Fermi

pockets: three spin-degenerate ones for each valley. At large enough doping, the triad of pockets for each valley and spin transforms into a single larger pocket, leaving four pockets, again valley and spin symmetric (Sym₄ state in Ref. [16] and in Fig. 3 (e)). The cascade of transitions happens in between these two limits, when the system develops particle-hole order that breaks valley and/or spin symmetry. We show the sequence of transitions in the cascade in the 2-patch model in Fig. 3.

The authors of [16, 17] detected the symmetric three intermediate phases, which they labeled IF₁, PIP₁, and PIP₂. The IF₁ state has one large pocket, the PIP₂ state has two large and two small pockets, and the intermediate PIP₁ state has one large and one small pocket. We argue that IF₁ is the state (i) in Eq. (4) with co-existing valley polarization and ferromagnetism in one valley. This order develops first and splits Fermi pockets in 1-3 fashion with one large pocket and three-fold degenerate small pockets, which may be present or sink below the Fermi level (panel (b) in Fig. 3). The PIP₂ is the state (ii) in Eq. (4) with either valley polarization or ferromagnetism in both valleys. This order develops at a larger magnitude of the order parameter and splits Fermi pockets into two large and two small pockets (panel (d) in Fig. 3). In the SU(4)-symmetric case there are three small pockets, but their number may be reduced by subleading interactions. The PIP₁ is the intermediate state (iii) in Eq. (4) with one large and one small pocket (panel (c) in Fig. 3). Experiments did not reveal the 1-3 state, which is the part of our theoretical sequence. We expect this state to be present, but probably in a narrow doping range. The spin-polarized correlated metal at the end of the cascade in Ref. [17] is a potential candidate for the 1-3 state. We also note that it depends on the size of the displacement field and the splitting on which side of the van Hove energy the Fermi level ends up after the transition to the 1-3, 2-2, and 3-1 states so that more phases are possible. This provides an explanation for the additional phases observed at larger displacement field in Ref. [17]. The data also show that in some range of displacement fields the system returns back to Sym₁₂ state in between PIP₁ and PIP₂. In our theory, this holds if particle-hole order vanishes in this parameter range.

DISCUSSION

In this theoretical work, we used as an input STM data for TBG, which show that upon electron or hole doping, one of the vH peaks in the DOS remains near the chemical potential in a wide range of fillings – between $|n| \lesssim 1$ and $|n| \lesssim 4$. We analyzed a cascade of phase transitions imposed by evolving spin/isospin order, which in turn is associated with the enhancement of the DOS for low-energy

fermions due to a confinement of a vH peak close to μ . We found a set of phase transitions: two first order transitions at $|n| \lesssim 1$ and $|n| \lesssim 4$ between disordered and ordered states and two transitions at $|n| \lesssim 2$ and $|n| \lesssim 3$ between different ordered states with different spin/isospin order and different splitting of vH peaks. These last transitions can be first order or continuous, via a narrow intermediate phase. We argue that these transitions give rise to the seesaw behavior of the compressibility, with the jumps of $d\mu/dn$ at the first-order transitions (where we also expect hysteretic behavior of the magnetization) and continuum, but rapid changes of $d\mu/dn$ if the transition is via an intermediate phase. We also emphasize that in our description the minima of $d\mu/dn$ are near, but not exactly at integer n .

The semi-phenomenological explanation of the cascade of transitions put forward in Ref. [15] assumes that at every transition one of 4 initially degenerate bands gets fully filled/fully emptied and no longer contributes to particle-hole order. Within this scenario, one can naturally explain the emergence of insulating states at integer fillings, but one would need to explain why the four vH peaks, seemingly moving to different energies as $|n|$ increases, recombine into a single vH peak at $|n| \lesssim 4$, as STM data show, and would also need to explain why the measured slope of $d\mu/dn$ does not scale inversely with the number of remaining peak components. We discuss this scenario in some detail in the Supplementary Discussion VIII. Interestingly, it yields the same ordered states as in our SU(4) scenario.

There is an element of phenomenology in our approach as well. Namely, we departed from a metal, associated the emergence of spin/isospin order with a vH singularity, and associated the cascade of transitions with near-integer $|n|$ based on STM data rather than on microscopic calculations. The confinement of transitions to integer $|n|$ and the emergence of insulating phases around these $|n|$ are most likely strong-coupling phenomena. We note in this regard that the SU(4)-symmetric Landau free energy, on which our results and the results of Ref. [15] are based upon, is in fact generic, and while we derived it from the specific microscopic itinerant model of interacting fermions with μ near the vH singularity, the same expression can be obtained in a strong coupling limit, where the bands are assumed to be nearly completely flat [15, 21, 53–56], and their internal structure does not play a role. Within the strong-coupling scenario, the STM peaks, which we interpreted as van Hove peaks, are treated as the peaks corresponding to flat bands. In either scenario, the Luttinger theorem states that the splitting due to spin/isospin orders can lead to the formation of insulating states only at integer fillings. A similar conclusion that a symmetry-breaking occurs at a non-integer filling due to vH physics and gives rise to an insulating behavior near integer n has been reached in Ref. [57]. In a recent experimental study [58]

the authors argued that the cascade of transitions in TBG is present in a range of twist angles, even when there are no insulating states near integer fillings. These results lend further support to our van Hove-based scenario of the cascade of phase transitions in TBG.

Our theory also describes the cascade of phase transitions, detected in compressibility and magnetoresistance measurements in BBG and RTG under a displacement field. These systems have small Fermi pockets near \mathbf{K} and \mathbf{K}' , which undergo a set of transitions around the vH doping. We argue that the splitting of the pockets in different phases in the cascade is the same as in TBG and is caused by the same set of valley and spin orders. The similarity of the cascade phases in TBG and BBG/RTG is quite striking given that BBG/RTG are substantially less correlated than TBG because an application of the displacement field flattens the dispersion near \mathbf{K} and \mathbf{K}' , but the full bandwidth remains the same as in the original non-twisted bilayer graphene. We believe that the similarity is an indication that the structure of particle-hole order in all three systems and the structure of the accompanied splitting of the electron bands can be understood already by analyzing what are the leading instabilities of a doped metal with valley and spin degrees of freedom. A strong coupling approach is certainly needed for the description of how in TBG the order creates an insulating behavior near integer fillings.

Acknowledgment We thank E. Berg, A. Cherman, Z. Dong, R. Fernandes, F. Guinea, J. Hoffman, S. Ilani, P. Jarillo-Herrero, E. König, C. Lewandowski, L. Levitov, Y. Oreg, H. Polshyn, G. Tarnopolsky, O. Vafek, A. Vishwanath, A. Yazdani, A. Young, and E. Zeldov for fruitful discussions. We are indebted to S. Ilani, K. Nuckolls, A. Yazdani, and U. Zondiner for sharing their data with us. The work by D.V.C and A.V.C. was supported by U.S. Department of Energy, Office of Science, Basic Energy Sciences, under Award No. DE-SC0014402. Y.W. was supported by NSF under award number DMR-2045781. D.V.C. gratefully acknowledges support from Doctoral Dissertation and Larkin Fellowships at the University of Minnesota.

Data availability Data will be kept in UMN database and will be available upon request.

Author contributions D.V.C. performed analytic calculations with an input from L.C., Y.W., and A.V.C. D.V.C. and A.V.C. wrote the first draft. All authors discussed the results and their relation to experiments, and contributed to writing the manuscript.

Competing interests The authors declare no competing interests.

-
- [1] Cao, Y. et al. Unconventional superconductivity in magic-angle graphene superlattices. Nature **556**, 43–50 (2018).
- [2] Yankowitz, M. et al. Tuning superconductivity in twisted bilayer graphene. Science **363**, 1059–1064 (2019).
- [3] Cao, Y. et al. Nematicity and competing orders in superconducting magic-angle graphene. Science **372**, 264–271 (2021).
- [4] Cao, Y. et al. Correlated insulator behaviour at half-filling in magic-angle graphene superlattices. Nature **556**, 80–84 (2018).
- [5] Xie, Y. et al. Spectroscopic signatures of many-body correlations in magic-angle twisted bilayer graphene. Nature **572**, 101–105 (2019).
- [6] Jiang, Y. et al. Charge order and broken rotational symmetry in magic-angle twisted bilayer graphene. Nature **573**, 91–95 (2019).
- [7] Chen, G. et al. Tunable correlated Chern insulator and ferromagnetism in a moiré superlattice. Nature **579**, 56–61 (2020).
- [8] Saito, Y. et al. Hofstadter subband ferromagnetism and symmetry-broken Chern insulators in twisted bilayer graphene. Nat. Phys. **17**, 478–481 (2021).
- [9] Xie, Y. et al. Fractional Chern insulators in magic-angle twisted bilayer graphene. Nature **600**, 439–443 (2021).
- [10] Sharpe, A. L. et al. Emergent ferromagnetism near three-quarters filling in twisted bilayer graphene. Science **365**, 605–608 (2019).
- [11] Serlin, M. et al. Intrinsic quantized anomalous Hall effect in a moiré heterostructure. Science **367**, 900–903 (2020).
- [12] Sharpe, A. L. et al. Evidence of orbital ferromagnetism in twisted bilayer graphene aligned to hexagonal boron nitride. Nano Lett. **21**, 4299–4304 (2021).
- [13] Tschirhart, C. L. et al. Imaging orbital ferromagnetism in a moiré Chern insulator. Science **372**, 1323–1327 (2021).
- [14] Wong, D. et al. Cascade of electronic transitions in magic-angle twisted bilayer graphene. Nature **582**, 198–202 (2020).

- [15] Zondiner, U. et al. Cascade of phase transitions and Dirac revivals in magic-angle graphene. Nature **582**, 203–208 (2020).
- [16] Zhou, H. et al. Isospin magnetism and spin-polarized superconductivity in Bernal bilayer graphene. Science **375**, 774–778 (2022).
- [17] Seiler, A. M. et al. Quantum cascade of correlated phases in trigonally warped bilayer graphene. Nature **608**, 298–302 (2022).
- [18] Zhou, H., Xie, T., Taniguchi, T., Watanabe, K. & Young, A. F. Superconductivity in rhombohedral trilayer graphene. Nature **598**, 434–438 (2021).
- [19] Zhou, H. et al. Half- and quarter-metals in rhombohedral trilayer graphene. Nature **598**, 429–433 (2021).
- [20] Li, G. et al. Observation of Van Hove singularities in twisted graphene layers. Nat. Phys. **6**, 109–113 (2010).
- [21] Kang, J., Bernevig, B. A. & Vafek, O. Cascades between light and heavy fermions in the normal state of magic-angle twisted bilayer graphene. Phys. Rev. Lett. **127**, 266402 (2021).
- [22] Park, J. M., Cao, Y., Watanabe, K., Taniguchi, T. & Jarillo-Herrero, P. Tunable strongly coupled superconductivity in magic-angle twisted trilayer graphene. Nature **590**, 249–255 (2021).
- [23] Liu, C.-C., Zhang, L.-D., Chen, W.-Q. & Yang, F. Chiral spin density wave and $d + id$ superconductivity in the magic-angle-twisted bilayer graphene. Phys. Rev. Lett. **121**, 217001 (2018).
- [24] Isobe, H., Yuan, N. F. Q. & Fu, L. Unconventional superconductivity and density waves in twisted bilayer graphene. Phys. Rev. X **8**, 041041 (2018).
- [25] González, J. & Stauber, T. Kohn-Luttinger superconductivity in twisted bilayer graphene. Phys. Rev. Lett. **122**, 026801 (2019).
- [26] Sherkunov, Y. & Betouras, J. J. Electronic phases in twisted bilayer graphene at magic angles as a result of Van Hove singularities and interactions. Phys. Rev. B **98**, 205151 (2018).
- [27] Ren, Y.-N. et al. Spectroscopic evidence for a spin- and valley-polarized metallic state in a nonmagic-angle twisted bilayer graphene. ACS Nano **14**, 13081–13090 (2020).
- [28] Chichinadze, D. V., Classen, L. & Chubukov, A. V. Valley magnetism, nematicity, and density wave orders in twisted bilayer graphene. Phys. Rev. B **102**, 125120 (2020).
- [29] Chichinadze, D. V., Classen, L., Wang, Y. & Chubukov, A. V. SU(4) symmetry in twisted bilayer graphene: An itinerant perspective. Phys. Rev. Lett. **128**, 227601 (2022).

- [30] Kang, J. & Vafek, O. Strong coupling phases of partially filled twisted bilayer graphene narrow bands. Phys. Rev. Lett. **122**, 246401 (2019).
- [31] Wang, Y., Kang, J. & Fernandes, R. M. Topological and nematic superconductivity mediated by ferro-SU(4) fluctuations in twisted bilayer graphene. Phys. Rev. B **103**, 024506 (2021).
- [32] Bultinck, N. et al. Ground state and hidden symmetry of magic-angle graphene at even integer filling. Phys. Rev. X **10**, 031034 (2020).
- [33] Xu, C. & Balents, L. Topological superconductivity in twisted multilayer graphene. Phys. Rev. Lett. **121**, 087001 (2018).
- [34] Venderbos, J. W. F. & Fernandes, R. M. Correlations and electronic order in a two-orbital honeycomb lattice model for twisted bilayer graphene. Phys. Rev. B **98**, 245103 (2018).
- [35] Classen, L., Honerkamp, C. & Scherer, M. M. Competing phases of interacting electrons on triangular lattices in moiré heterostructures. Phys. Rev. B **99**, 195120 (2019).
- [36] Natori, W. M. H., Nutakki, R., Pereira, R. G. & Andrade, E. C. SU(4) Heisenberg model on the honeycomb lattice with exchange-frustrated perturbations: Implications for twistrionics and Mott insulators. Phys. Rev. B **100**, 205131 (2019).
- [37] Seo, K., Kotov, V. N. & Uchoa, B. Ferromagnetic Mott state in twisted graphene bilayers at the magic angle. Phys. Rev. Lett. **122**, 246402 (2019).
- [38] Cea, T., Walet, N. R. & Guinea, F. Electronic band structure and pinning of Fermi energy to Van Hove singularities in twisted bilayer graphene: A self-consistent approach. Phys. Rev. B **100**, 205113 (2019).
- [39] Rademaker, L., Abanin, D. A. & Mellado, P. Charge smoothening and band flattening due to Hartree corrections in twisted bilayer graphene. Phys. Rev. B **100**, 205114 (2019).
- [40] Guinea, F. & Walet, N. R. Electrostatic effects, band distortions, and superconductivity in twisted graphene bilayers. Proc. Natl. Acad. Sci. U.S.A. **115**, 13174–13179 (2018).
- [41] Wagner, G., Kwan, Y. H., Bultinck, N., Simon, S. H. & Parameswaran, S. A. Global phase diagram of the normal state of twisted bilayer graphene. Phys. Rev. Lett. **128**, 156401 (2022).
- [42] Note, that the expression here uses a slightly different definition of prefactors in the free energy than the one in [29].
- [43] Hamermesh, M. Group theory and its application to physical problems (Courier Corporation, 2012).

- [44] Kang, J. & Vafeek, O. Symmetry, maximally localized Wannier states, and a low-energy model for twisted bilayer graphene narrow bands. Phys. Rev. X **8**, 031088 (2018).
- [45] Yuan, N. F. Q. & Fu, L. Model for the metal-insulator transition in graphene superlattices and beyond. Phys. Rev. B **98**, 045103 (2018).
- [46] Castro, E. V. et al. Biased bilayer graphene: Semiconductor with a gap tunable by the electric field effect. Phys. Rev. Lett. **99**, 216802 (2007).
- [47] McCann, E. & Fal'ko, V. I. Landau-level degeneracy and quantum Hall effect in a graphite bilayer. Phys. Rev. Lett. **96**, 086805 (2006).
- [48] Castro Neto, A. H., Guinea, F., Peres, N. M. R., Novoselov, K. S. & Geim, A. K. The electronic properties of graphene. Rev. Mod. Phys. **81**, 109–162 (2009).
- [49] McCann, E. & Koshino, M. The electronic properties of bilayer graphene. Rep. Prog. Phys. **76**, 056503 (2013).
- [50] Koshino, M. & McCann, E. Trigonal warping and Berry's phase $N\pi$ in ABC-stacked multilayer graphene. Phys. Rev. B **80**, 165409 (2009).
- [51] Zhang, F., Sahu, B., Min, H. & MacDonald, A. H. Band structure of ABC-stacked graphene trilayers. Phys. Rev. B **82**, 035409 (2010).
- [52] Ghazaryan, A., Holder, T., Serbyn, M. & Berg, E. Unconventional superconductivity in systems with annular Fermi surfaces: Application to rhombohedral trilayer graphene. Phys. Rev. Lett. **127**, 247001 (2021).
- [53] Vafeek, O. & Kang, J. Renormalization group study of hidden symmetry in twisted bilayer graphene with Coulomb interactions. Phys. Rev. Lett. **125**, 257602 (2020).
- [54] Khalaf, E., Bultinck, N., Vishwanath, A. & Zaletel, M. P. Soft modes in magic angle twisted bilayer graphene (2020). URL <https://arxiv.org/abs/2009.14827>.
- [55] Lian, B. et al. Twisted bilayer graphene. IV. Exact insulator ground states and phase diagram. Phys. Rev. B **103**, 205414 (2021).
- [56] Ledwith, P. J., Khalaf, E. & Vishwanath, A. Strong coupling theory of magic-angle graphene: A pedagogical introduction. Ann. Phys. (N. Y.) **435**, 168646 (2021). Special issue on Philip W. Anderson.
- [57] Xie, M. & MacDonald, A. H. Weak-field Hall resistivity and spin-valley flavor symmetry breaking in magic-angle twisted bilayer graphene. Phys. Rev. Lett. **127**, 196401 (2021).

- [58] Polski, R. et al. Hierarchy of symmetry breaking correlated phases in twisted bilayer graphene (2022). URL <https://arxiv.org/abs/2205.05225>.
- [59] Chen, N., Rytov, T. A. & Shrock, R. Patterns of dynamical gauge symmetry breaking. Phys. Rev. D **82**, 116006 (2010).
- [60] Wu, S., Zhang, Z., Watanabe, K., Taniguchi, T. & Andrei, E. Y. Chern insulators, van hove singularities and topological flat bands in magic-angle twisted bilayer graphene. Nature Materials **20**, 488–494 (2021).
- [61] Lemonik, Y., Aleiner, I. & Fal'ko, V. I. Competing nematic, antiferromagnetic, and spin-flux orders in the ground state of bilayer graphene. Phys. Rev. B **85**, 245451 (2012).
- [62] Cvetkovic, V., Throckmorton, R. E. & Vafeek, O. Electronic multicriticality in bilayer graphene. Phys. Rev. B **86**, 075467 (2012).
- [63] Dong, Z., Chubukov, A. V. & Levitov, L. Spin-triplet superconductivity at the onset of isospin order in biased bilayer graphene (2022). URL <https://arxiv.org/abs/2205.13353>.

Supplemental Material

SUPPLEMENTARY DISCUSSION I: THE GROUND STATE OF AN SU(4)-SYMMETRIC FREE ENERGY

In the main text we discuss an effective model of fermions near six (or twelve) van Hove points in twisted bilayer graphene (TBG). The model consists of 4 sets of interacting fermions (2 spin and 2 valley isospin variables). We argued previously [29] that in both cases (six or twelve van Hove points) there are 15 particle-hole order parameters (bilinear combinations of fermions) with nearly equal attractive couplings. The couplings for other order parameters are either repulsive or smaller by magnitude. More precisely, the set of 15 consists of two subsets of 7 and 8 bilinears. The couplings within each subset are identical (λ_7 for the first subset, λ_8 for the second). The couplings λ_7 and λ_8 are not identical, but are close to each other, and in our analysis we treated them as equal. These 15 fermionic bilinears then form an adjoint representation of the SU(4) group. Here we analyze in some detail the Landau free energy of the corresponding SU(4) model and obtain the structure of the ordered state for different parameters. For completeness, we also analyze the structure of the order in SU(N) models with $N = 3$, which in our case are effective models of fermions with 3 degenerate bands and $N^2 - 1 = 8$ particle-hole bilinears with equal couplings (see Supplementary Discussion VI below). It is convenient to consider the general SU(N) case for the free energy and specify $N = 4$ or $N = 3$ in the next section.

The free energy of a system of $N^2 - 1$ degenerate particle-hole order parameters ϕ_i is, to fourth order in ϕ_i

$$\mathcal{F} = -\frac{\alpha}{2}\text{Tr}[\hat{\Phi}^2] + \frac{\gamma}{3}\text{Tr}[\hat{\Phi}^3] + \frac{\beta}{4}\text{Tr}[\hat{\Phi}^4] + \frac{\beta'}{4}\text{Tr}[\hat{\Phi}^2]^2. \quad (\text{S1})$$

Here $\hat{\Phi} = \sum_j^{N^2-1} \phi_j T^j$, where T^j are the generators of the group SU(N). Note, that the prefactors in the free energy are defined in a slightly different way than in [29]. The order-parameter fields ϕ_j are expressed via fermionic bilinears as

$$\phi_j \sim f^\dagger T^j f \quad (\text{S2})$$

where f^\dagger and f are electronic creation and annihilation operators. The momentum-transfer between electrons can be zero or finite depending on which order ϕ_j corresponds to.

This effective model can be straightforwardly obtained by departing from the Hamiltonian for N

species with equal dispersion and 4-fermion interactions, selecting $N^2 - 1$ particle-hole bilinears, applying a Hubbard-Stratonovich transformation, and integrating out the fermions. Note that in the effective model we considered previously [29], the dispersion of all fermion species was non-degenerate for different valleys so that the $SU(4)$ symmetry was only approximate. The β' -term in (S1) does not appear in the expansion of the logarithm in the Hubbard-Stratonovich formalism, but is allowed on general grounds and in practice is generated in the renormalization group flow [59]. This term and the β term are the two independent quartic terms for $N = 4$. For $N = 3$, $\text{Tr}[\hat{\Phi}^2]^2 = 2\text{Tr}[\hat{\Phi}^4]$, in which case the two terms are equivalent and we can β' into β .

In the Hubbard-Stratonovich formalism the sign of γ is determined by the sign of a one-loop diagram with three fermion-boson vertices and three propagators of low-energy fermions. The diagram vanishes in the limit when there is a particle-hole symmetry around the Fermi surface, but is non-zero in a generic case. For definiteness, below we set $\gamma > 0$. The extension to the case $\gamma < 0$ changes the overall sign of the order parameter.

Because $\hat{\Phi}$ is in the adjoint representation of the $SU(N)$ group, it can be represented by a traceless matrix [43]. It is convenient to apply a unitary transformation and analyze $\hat{\Phi}$ in the diagonal basis, where it takes the form

$$\hat{\Phi} = \text{diag}(\lambda_1, \lambda_2, \dots, \lambda_{N-1}, -(\lambda_1 + \dots + \lambda_{N-1})). \quad (\text{S3})$$

In this representation the free energy (S1) reads

$$\begin{aligned} \mathcal{F} = & -\frac{\alpha}{2} \left(\sum_j^{N-1} \lambda_j^2 + \left(\sum_j^{N-1} \lambda_j \right)^2 \right) + \frac{\gamma}{3} \left(\sum_j^{N-1} \lambda_j^3 - \left(\sum_j^{N-1} \lambda_j \right)^3 \right) \\ & + \frac{\beta}{4} \left(\sum_j^{N-1} \lambda_j^4 + \left(\sum_j^{N-1} \lambda_j \right)^4 \right) + \frac{\beta'}{4} \left(\sum_j^{N-1} \lambda_j^2 + \left(\sum_j^{N-1} \lambda_j \right)^2 \right)^2. \end{aligned} \quad (\text{S4})$$

Note that the first three terms in (S4) have the form of

$$\frac{\varkappa_n}{n} \left(\sum_j^{N-1} \lambda_j^n + (-1)^n \left(\sum_j^{N-1} \lambda_j \right)^n \right), \quad (\text{S5})$$

where $\varkappa_n \in \{\alpha, \beta, \gamma\}$. Below we explicitly minimize the free energy (S4) for $N = 4, 3, 2$. For definiteness we assume that the prefactor α in (S4) is positive and analyze energy minimization for finite λ_j . The combination of stationary non-zero λ_j determines the type of order in terms of fermion bilinears $\phi_j \sim \langle f^\dagger T^j f \rangle$ and also determines the shift of the van Hove peaks of reconstructed energy bands.

For $N = 4$ the order parameter matrix $\hat{\Phi}$ in the diagonal basis is

$$\hat{\Phi} = \text{diag}(\lambda_1, \lambda_2, \lambda_3, -(\lambda_1 + \lambda_2 + \lambda_3)). \quad (\text{S6})$$

The free energy (S4) is then a function of three parameters $\lambda_{1,2,3}$. The values of these parameters are determined by the condition that the free energy is at a minimum. We analyze the solutions of $\frac{\partial F}{\partial \lambda_l} = 0$. In explicit form

$$\frac{\partial F}{\partial \lambda_l} = -\alpha \left(\lambda_l + \sum_j \lambda_j \right) + \gamma \left[\lambda_l^2 - \left(\sum_j \lambda_j \right)^2 \right] + \beta \left[\lambda_l^3 + \left(\sum_j \lambda_j \right)^3 \right] + \beta' \left[\sum_j \lambda_j^2 + \left(\sum_j \lambda_j \right)^2 \right] \left(\lambda_l + \sum_k \lambda_k \right) = 0 \quad (\text{S7})$$

In our previous work [29] we set $\gamma = \beta' = 0$ and found two solutions: $\lambda_1 = \lambda_2 = -\lambda_3 = (\alpha/\beta)^{1/2}$ and $\lambda_1 = \lambda_2 = \lambda_3 = (\alpha/(7\beta))^{1/2}$. For the first solution a 4-fold degenerate van Hove level splits into two doubly degenerate levels, for the second one the van Hove level splits into one 3-fold degenerate level and one single level. The first solution has lower free energy, hence the only option at $\gamma = \beta' = 0$ is 2-2 splitting.

For a generic case when γ and β' are non-zero, we subtract Eq. (S7) for $l = 2$ from that for $l = 1$ and obtain

$$0 = (\lambda_1 - \lambda_2) \left[-\alpha + \gamma(\lambda_1 + \lambda_2) + \beta(\lambda_1^2 + \lambda_1\lambda_2 + \lambda_2^2) + \beta' \left(\sum_j \lambda_j^2 + \left(\sum_j \lambda_j \right)^2 \right) \right]. \quad (\text{S8})$$

We see that either $\lambda_1 = \lambda_2$ or the λ 's have to satisfy the quadratic equation in square brackets in (S8). Below we search for the solutions of (S7) with the constraint $\lambda_1 = \lambda_2$. It is straightforward to verify that enforcing instead the condition set by the quadratic equation in (S8) ultimately leads to the same solutions with permuted λ_j .

Let us label $\lambda_1 = \lambda_2 = \lambda$. The remaining two equations in (S7) are

$$\begin{aligned} 0 &= 2(\lambda + \lambda_3) \left(-\alpha - 2\gamma\lambda + \beta(4\lambda^2 + 2\lambda\lambda_3 + \lambda_3^2) + 2\beta'(3\lambda^2 + \lambda_3^2 + 2\lambda\lambda_3) \right) \\ 0 &= (\lambda - \lambda_3) \left(-\alpha + \gamma(\lambda + \lambda_3) + \beta(\lambda^2 + \lambda\lambda_3 + \lambda_3^2) + 2\beta'(3\lambda^2 + \lambda_3^2 + 2\lambda\lambda_3) \right) \end{aligned} \quad (\text{S9})$$

The upper equation follows from (S7) for $l = 3$ and the lower one is obtained by subtracting the equation for $l = 3$ from that for $l = 1$. There are three possible solutions of these equations: (i) $\lambda = \lambda_3$,

where λ is determined by the second bracket in the first equation; (ii) $\lambda = -\lambda_3$, where λ is determined by the second bracket in the second equation; (iii) λ and λ_3 are different and are determined by second brackets in both equations. Let us consider those conditions one by one.

(i) $\lambda = \lambda_3$. Solving for λ , we obtain

$$\lambda = \frac{\gamma + \sqrt{\gamma^2 + \alpha(7\beta + 12\beta')}}{7\beta + 12\beta'} \quad (\text{S10})$$

The free energy at the minimum is given by

$$\mathcal{F} = \frac{\alpha^2}{\beta} f_i(x, y), \quad (\text{S11})$$

where $x = \frac{\gamma}{\sqrt{\alpha\beta}}$, $y = \beta'/\beta$, and

$$f_i(x, y) = \frac{(x + \sqrt{7 + x^2 + 12y})^2 \left[3(7 + 12y) + 2x(x + \sqrt{7 + x^2 + 12y}) \right]}{(7 + 12y)^3}. \quad (\text{S12})$$

If $\gamma < 0$, the solution with a minus sign in front of the square roots in Eqs. (S10)+(S12) corresponds to a minimum.

(ii) $\lambda = -\lambda_3$. In this case

$$\lambda = \sqrt{\frac{\alpha}{\beta(1 + 4y)}}, \quad (\text{S13})$$

and

$$\mathcal{F} = \frac{\alpha^2}{\beta} f_{ii}(x, y). \quad (\text{S14})$$

where

$$f_{ii}(x, y) = -\frac{1}{1 + 4y} \quad (\text{S15})$$

Note that f_{ii} is independent of x .

(iii) λ and λ_3 are determined by the two quadratic equations:

$$\begin{aligned} 0 &= -\alpha + \gamma(\lambda + \lambda_3) + \beta(\lambda^2 + \lambda\lambda_3 + \lambda_3^2) + 2\beta'(3\lambda^2 + \lambda_3^2 + 2\lambda\lambda_3) \\ 0 &= -\alpha - 2\gamma\lambda + \beta(4\lambda^2 + 2\lambda\lambda_3 + \lambda_3^2) + 2\beta'(3\lambda^2 + \lambda_3^2 + 2\lambda\lambda_3) \end{aligned} \quad (\text{S16})$$

Subtracting one from the other we obtain

$$(3\lambda + \lambda_3)(\gamma - \beta\lambda) = 0. \quad (\text{S17})$$

The solution $\lambda_3 = -3\lambda$ brings us back to case (i). The other solution is

$$\lambda = \frac{\gamma}{\beta}$$

$$\lambda_3 = -\frac{\gamma}{\beta} \pm \sqrt{\frac{\frac{\alpha}{\beta} - \frac{\gamma^2}{\beta^2} \left(1 + 4\frac{\beta'}{\beta}\right)}{1 + 2\frac{\beta'}{\beta}}} \quad (\text{S18})$$

This solution exists only for $|x| \leq 1/\sqrt{1+4y}$. The corresponding free energy is

$$\mathcal{F} = \frac{\alpha^2}{\beta} f_{iii}(x, y) \quad (\text{S19})$$

where

$$f_{iii}(x, y) = -\frac{1 + 2x^2 - x^4(1 + 4y)}{2(1 + 2y)} \quad (\text{S20})$$

Note that the free energy is the same for both signs in front of the square root in Eq. (S18).

The solution (iii) merges with the solution (ii) at $|x| = 1/\sqrt{1+4y}$, where $\lambda_3 = -\lambda$ and with the solution (i) at a smaller $|x| = 1/\sqrt{5+12y}$ where $\lambda_3 = \lambda$ or -3λ , depending on the sign in front of the square root in (S18).

We plot $f_l(x, y)$ ($l = i, ii, iii$) in Fig. 2 of the main text as function of x for $y = 0$ and $y = 1$. In both cases, for large x (small positive α at a non-zero γ), the smallest free energy is for the state (i), and for small x (small γ and a finite α) the smallest free energy is for the state (ii). The intermediate state (iii) is never a minimum of \mathcal{F} . This means that there is a direct first-order transition between states (i) and (ii) at some critical x_{cr} . This result holds for all y . Still, $f_{iii}(x, y)$ is close to $f_i(x, y)$ and $f_{ii}(x, y)$ near where they become equal, particularly at large y . It is then entirely possible that f_{iii} becomes the ground state near x_{cr} if we move the system away from SU(4) symmetry by, e.g., adding interaction terms which scatter between valleys. In this case the transition from state (i) at large x to state (ii) at small x becomes a continuous one via an intermediate phase.

SUPPLEMENTARY DISCUSSION II: SYMMETRY PROPERTIES

(i) $\lambda = \lambda_3$. In the diagonal basis, the matrix $\hat{\Phi}$ is

$$\hat{\Phi} = \text{diag}(\lambda, \lambda, \lambda, -3\lambda), \quad (\text{S21})$$

The remnant symmetry of this state is $\text{SU}(3) \times \text{U}(1)$, which is a subgroup of the original SU(4) symmetry group. Here, SU(3) corresponds to symmetry transformations in the subspace of the first three

components of $\hat{\Phi}$ and U(1) to a relative phase variation between the last and the first three components. Up to rotations of the overall phase, the SU(3) and U(1) generators are given by block-diagonal matrices

$$U_{\text{SU}(3)} = \text{diag}(e^{i\alpha_i T^i}, 1), \quad U_{\text{U}(1)} = \text{diag}(\mathbb{1}_3, e^{i\theta}) \quad (\text{S22})$$

where $T^i, i = 1, \dots, 8$ are eight Gell-Mann matrices, and $\mathbb{1}$ is a 3×3 identity matrix. It can be explicitly checked that transformation matrices $U_{\text{SU}(3)}$ and $U_{\text{U}(1)}$ commute with the order parameter matrix $\hat{\Phi}$, therefore, the symmetry of the ground state is SU(3) \times U(1).

(ii) $\lambda = -\lambda_3$. The matrix $\hat{\Phi}$ is

$$\hat{\Phi} = \text{diag}(\lambda, \lambda, -\lambda, -\lambda) \quad (\text{S23})$$

The remnant symmetry of this state is SU(2) \times SU(2) \times U(1), where the two SU(2)'s correspond to rotations within the subsets of the first two and the last two components of $\hat{\Phi}$, and U(1) corresponds to a rotation of one subset relative to the other. They can be represented by

$$\begin{aligned} U_{\text{SU}(2)} &= \text{diag}(e^{i\alpha_i \sigma^i}, \mathbb{1}_2) \\ U'_{\text{SU}(2)} &= \text{diag}(\mathbb{1}_2, e^{i\alpha_i \sigma^i}) \\ U_{\text{U}(1)} &= \text{diag}(\mathbb{1}_2, e^{i\theta} \mathbb{1}_2), \end{aligned} \quad (\text{S24})$$

where σ^i are the Pauli matrices.

(iii) $\lambda \neq \pm\lambda_3$. The matrix $\hat{\Phi}$ is

$$\text{diag}(\lambda, \lambda, -\lambda_3, -2\lambda + \lambda_3) \quad (\text{S25})$$

The remnant symmetry of this state is SU(2) \times U(1) \times U(1), where SU(2) correspond to rotations within the subsets of the first two components and the two U(1)'s corresponds to independent, relative rotations of the third and the fourth components, e.g.,

$$\begin{aligned} U_{\text{SU}(2)} &= \text{diag}(e^{i\alpha_i \sigma^i}, \mathbb{1}_2) \\ U_{\text{U}(1)} &= \text{diag}(\mathbb{1}_2, e^{i\theta}, 1) \\ U'_{\text{U}(1)} &= \text{diag}(\mathbb{1}_2, 1, e^{i\theta}). \end{aligned} \quad (\text{S26})$$

SUPPLEMENTARY DISCUSSION III: RELAXING SU(4) SYMMETRY

As we mentioned at the beginning, the 15 order parameters with near-equal, attractive couplings near van Hove filling consist of two subsets with seven intra-valley, $Q = 0$ order parameters and eight inter-valley, $Q \neq 0$ order parameters. The set with seven order parameters is described by the order parameter matrix $\hat{\Phi}_7 = \sum \varphi_{ij}^{(7)} \sigma_i \tau_j$ with $i = 0, \dots, 3$, $j = 0, 3$, excluding $i = j = 0$, and σ_i (τ_j) are Pauli matrices for (iso-)spin degrees of freedom, where $\sigma_0 = \tau_0 = \mathbb{1}_2$. The set with eight order parameters is described by $\hat{\Phi}_8 = \sum \varphi_{ij}^{(8)} \sigma_i \tau_j$ with $i = 0, \dots, 3$ and $j = 1, 2$ [29]. There is a single coupling constant within each set (λ_7 and λ_8 , respectively). In the microscopic model that we used to derive the free energy, λ_7 and λ_8 are close in magnitude. In our analysis above, we neglected the difference between these two couplings, in which case the free energy is SU(4)-symmetric.

Here we briefly analyze what happens if we do not treat λ_7 and λ_8 as equal and instead assume that one of the two is larger and the order is formed within either the set of 7 or the set of 8. Keeping only one of the sets, integrating out fermion fields, and approximating the bare Green's functions for all spins and isospins to be equal, we obtain again the free energy in the form

$$\mathcal{F}_\mu = -\frac{\alpha}{2} \text{Tr}[\hat{\Phi}_\mu^2] + \frac{\gamma}{3} \text{Tr}[\hat{\Phi}_\mu^3] + \frac{\beta}{4} \text{Tr}[\hat{\Phi}_\mu^4] \quad (\text{S27})$$

with $\mu = 7, 8$. Here we neglect any symmetry-allowed terms that are not produced by integrating out the fermions and appear as higher-order effects.

Diagonalization of $\hat{\Phi}_\mu$ shows that

$$\hat{\Phi}_7 \sim \text{diag}[\lambda_1, \lambda_2, \lambda_3, -(\lambda_1 + \lambda_2 + \lambda_3)] \quad (\text{S28})$$

$$\hat{\Phi}_8 \sim \text{diag}[\lambda_1, -\lambda_1, \lambda_2, -\lambda_2]. \quad (\text{S29})$$

Using this in Eq. (S27), we obtain for \mathcal{F}_7 the same expression as in the SU(4) symmetric case. Thus, within the set of 7 intra-valley $Q = 0$ order parameters one obtains the same ordered states as in SU(4)-symmetric model, and hence the same sequence of splittings of vH peak components (1-3 (3-1) and 2-2) and the same cascade of transitions. The remaining symmetries of the ordered states differ from the ones in the case with full SU(4) symmetry since $\text{SU}(2) \times \text{SU}(2) \times \text{U}(1)$ is already a subgroup of SU(4). In the reduced symmetry case the first transition ($n = 1$) gives $\text{SU}(2) \times \text{U}(1)$ residual symmetry, the second transition ($n = 2$) leads to SU(2) residual symmetry, which can be either spin or valley, depending on the realization of the ground state.

For the set of 8 inter-valley order parameters $\text{Tr}[\hat{\Phi}_\mu^3]$ vanishes. Then the ordered state gives rise to only 2 – 2 splitting of vH peaks. There is no phases with 1-3 (3-1) splitting and, hence, no cascade of transitions.

SUPPLEMENTARY DISCUSSION IV: THE GROUND STATE OF AN SU(3)-SYMMETRIC FREE ENERGY

We next consider the case of an SU(3)-symmetric free energy. Such a symmetry of fermionic bilinears can emerge when there are three degenerate bands near van Hove points (this is the case when the dispersion of one of the initially 4 degenerate bands shifts such that the whole band moves away from the chemical potential). Like we said, for the $N = 3$ case one can set $\beta' = 0$ without losing generality.

In the SU(3)-symmetric case the order parameter matrix reads

$$\hat{\Phi} = \text{diag}(\lambda_1, \lambda_2, -(\lambda_1 + \lambda_2)) \quad (\text{S30})$$

and the conditions for extrema are

$$-\alpha(2\lambda_1 + \lambda_2) + \gamma(\lambda_1^2 - (\lambda_1 + \lambda_2)^2) + \beta(\lambda_1^3 + (\lambda_1 + \lambda_2)^3) = 0, \quad (\text{S31})$$

$$-\alpha(2\lambda_2 + \lambda_1) + \gamma(\lambda_2^2 - (\lambda_1 + \lambda_2)^2) + \beta(\lambda_2^3 + (\lambda_1 + \lambda_2)^3) = 0. \quad (\text{S32})$$

Subtracting one equation from the other, we obtain that either $\lambda_1 = \lambda_2$, or $-\alpha - \gamma(\lambda_1 + \lambda_2) + \beta(\lambda_1^2 + \lambda_2^2 + \lambda_1\lambda_2) = 0$. In the first case, $\hat{\Phi} = \text{diag}(\lambda, \lambda, -2\lambda)$, where

$$\lambda = \frac{\gamma \pm \sqrt{12\alpha\beta + \gamma^2}}{6\beta}. \quad (\text{S33})$$

The free energy is

$$F = -\frac{\alpha^2}{\beta} g(x), \quad (\text{S34})$$

with

$$g(x) = \frac{(x \pm \sqrt{12 + x^2})^2 (18 + x(x \pm \sqrt{12 + x^2}))}{432}. \quad (\text{S35})$$

The choice of \pm in (S33),(S35) depends on the sign of γ .

We analyzed the second condition, $-\alpha - \gamma(\lambda_1 + \lambda_2) + \beta(\lambda_1^2 + \lambda_2^2 + \lambda_1\lambda_2) = 0$, and found that it yields $\lambda_2 = -2\lambda_1$, i.e., $\hat{\Phi} = \text{diag}(\lambda, -2\lambda, \lambda)$. This is the same $\hat{\Phi}'$ as above, up to permutations of the components. Accordingly, λ and the free energy are the same as in (S35).

We argue therefore that in the SU(3) model the ordered state is the same for all $|x|$. This is the key distinction from the SU(4) model, where the ordered state changes between large and small $|x|$.

The remnant symmetry of the system in the ordered state is $SU(2) \times U(1)$. Here, SU(2) corresponds to symmetry transformations for the first two components of $\hat{\Phi} = \text{diag}(\lambda, \lambda, -2\lambda)$ and U(1) corresponds to a relative phase variation between the first two and the last components.

SUPPLEMENTARY DISCUSSION V: EXAMPLE CALCULATION FOR A VAN HOVE PEAK

We consider a generic dispersion around a van Hove point of the form $\xi(\mathbf{k}) = \epsilon(\mathbf{k}) - \mu$ with $\epsilon(\mathbf{k}) = k_x^2 - k_y^2$ and $-t \leq \xi \leq t$. The filling for given chemical potential is given by

$$\begin{aligned} n(\mu) &= \int d^2k n_F(\xi(\mathbf{k})) \\ &= \frac{t\pi}{2} + \mu \text{arccoth} \frac{t}{\sqrt{t^2 - \mu^2}} + t \arctan \frac{\mu}{\sqrt{t^2 - \mu^2}} \end{aligned} \quad (\text{S36})$$

with Fermi function n_F . This can also be expressed as

$$n(\mu) = T \sum_{i\omega} \int d^2k G_0(i\omega, \mathbf{k}), \quad (\text{S37})$$

where $G_0 = (i\omega - \xi)^{-1}$ is the single-particle Green's function. Thus, the cubic coefficient γ can be related to the single-particle density via

$$\begin{aligned} \gamma &= -T \sum_{i\omega} \int d^2k G_0^3(i\omega, \mathbf{k}) \\ &= -\frac{1}{2} \frac{d^2 n}{d\mu^2}. \end{aligned} \quad (\text{S38})$$

This formula works at some distance from the van Hove point but not in its immediate vicinity because to derive it we interchanged integration and differentiation. This procedure is not valid at the van Hove point due to the singularity. We show the density n and its derivatives, including γ , in Fig. S1. We see the expected sign change of γ before and after the van Hove point. This behavior is generic around van Hove filling because the slope of the inverse compressibility $d\mu/dn$ changes sign at the van Hove point. In Fig. S2 we sketch how the Landau free energy parameters depend on electron filling.

In the main text we argue that, as the system approaches the van Hove energy at increasing doping, the van Hove peak is split in a first-order transition. As an example for the splitting, we consider

an order parameter S , which splits the dispersion to $\epsilon_s(\mathbf{k}) = k_x^2 - k_y^2 \pm S$. This happens e.g., due to ferromagnetic order in both valleys around $n \approx 2$, that leads to the 2-2 splitting. We calculate the corresponding inverse compressibility in Fig. S3. An analogous behavior occurs at each of the transitions of the cascade, which reproduces to the seesaw behavior, observed in the measured compressibility (Fig. 1 of the main text).

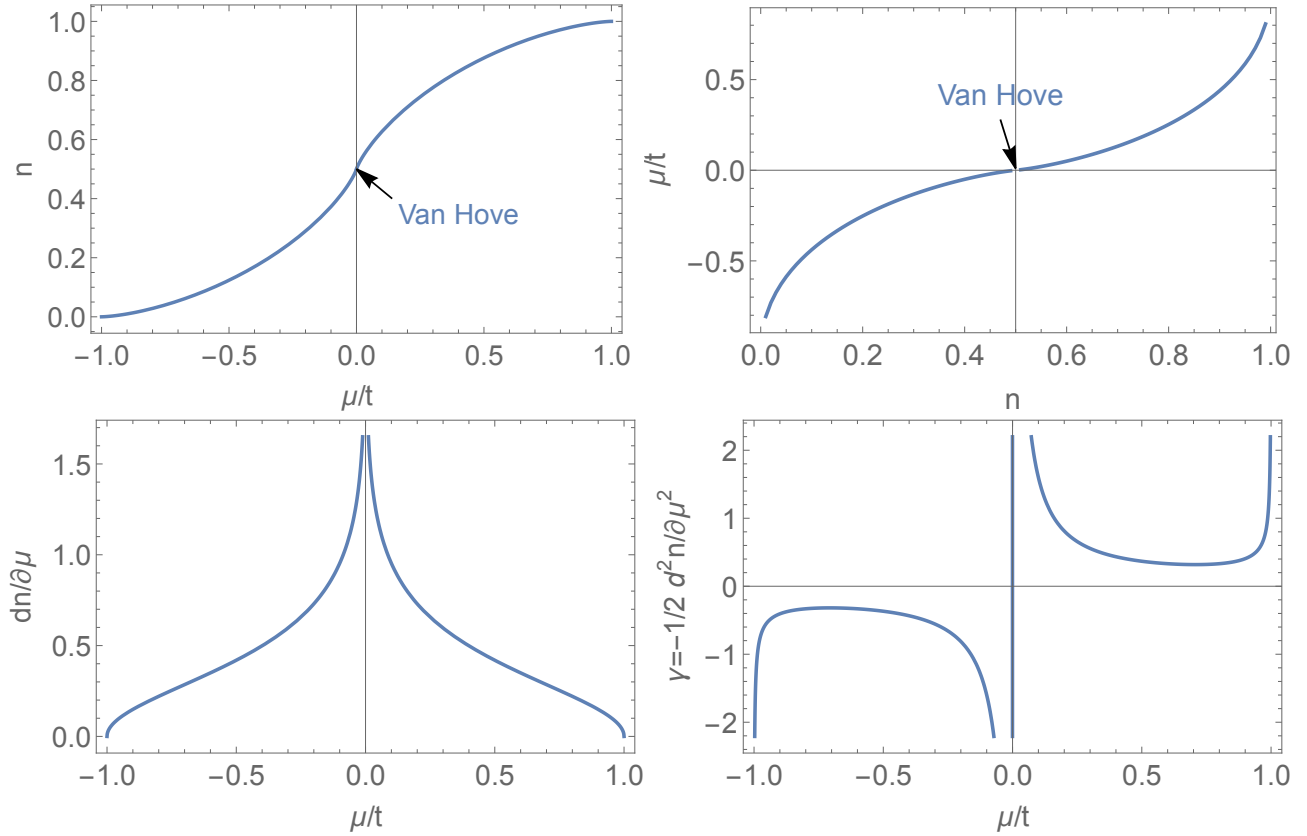


FIG. S1. Density n as function of chemical potential μ according to Eq. (S36) (top left) and conversely chemical potential as function of filling. The first derivatives of n determines the compressibility (bottom left) and the second derivative the bare cubic coefficient γ in the free energy.

SUPPLEMENTARY DISCUSSION VI: DERIVATION OF SU(3)-SYMMETRIC LANDAU FUNCTIONAL FROM THE MICROSCOPIC 6-PATCH MODEL

Here we show how the SU(3) symmetry appears in the 6-patch model in the case of one valley hosting electrons with only one spin projection. The sketch of patch structure, momentum transfer

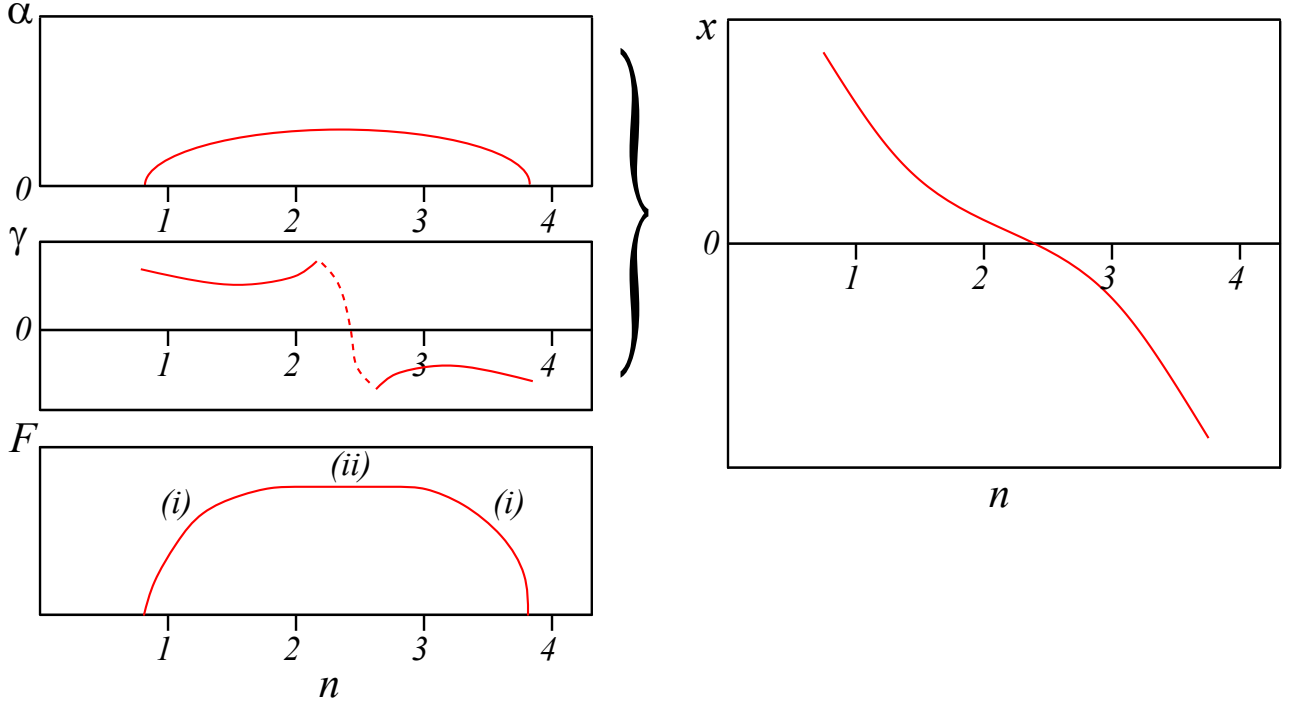


FIG. S2. Illustrative sketch of the behavior of α , γ , x as a function of filling n . The lowest picture illustrates the correspondence between the minima of the free energy and filling n .

vectors, and interactions is given in Fig. S4. Density-density interactions between each patch are identical, exchange interaction is allowed if fermions do not change their valley in the process of scattering. The coupling constants and polarization operators are the same as in the full 6-patch model with vH singularities of all 4 bands at the Fermi level. Every patch in the model we consider here is valley-polarized and one of the valleys is also spin-polarized. We label patches by $i = 1, 2, 3$ for valley + and by $i' = 1, 2, 3$ for valley -, spins by $s, s' = \uparrow, \downarrow$ and consider valley - as spinless, i.e., having only one spin projection. For the interaction we use the same model as in Ref. [28] with density-density and exchange couplings u and j .

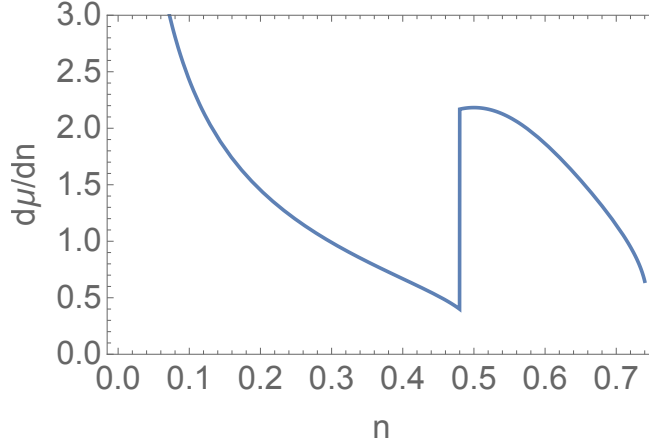


FIG. S3. Inverse compressibility as function of density n assuming a first order transition that splits the van Hove peak according to $\epsilon_S(\mathbf{k}) = k_x^2 - k_y^2 \pm S$. We use $S = 0.4$ for $n \geq 0.48$.

We introduce all possible order parameters involving fermions near vH points:

$$\begin{aligned}
\Delta_{Pom,+i}^c &= \langle f_{+,s,i}^\dagger \delta_{ss'} f_{+,s',i} \rangle, \\
\Delta_{Pom,+i}^s &= \langle f_{+,s,i}^\dagger \boldsymbol{\sigma}_{ss'} f_{+,s',i} \rangle, \\
\Delta_{Pom,-i'} &= \langle f_{-,i'}^\dagger f_{-,i'} \rangle, \\
\Delta_{Q_{s,+,-,\uparrow},i} &= \langle f_{+,\uparrow,(i+2)}^\dagger f_{-, (i+1)'} \rangle, \\
\Delta_{Q_{s,+,-,\uparrow},i'} &= \langle f_{+,\uparrow,(i+1)}^\dagger f_{-, (i+2)'} \rangle, \\
\Delta_{Q_{s,+,-,\downarrow},i} &= \langle f_{+,\downarrow,(i+2)}^\dagger f_{-, (i+1)'} \rangle, \\
\Delta_{Q_{s,+,-,\downarrow},i'} &= \langle f_{+,\downarrow,(i+1)}^\dagger f_{-, (i+2)'} \rangle, \\
\Delta_{Q_m,+i}^c &= \langle f_{+,s,i+2}^\dagger \delta_{ss'} f_{+,s',i+1} \rangle, \\
\Delta_{Q_m,+i}^s &= \langle f_{+,s,i+2}^\dagger \boldsymbol{\sigma}_{ss'} f_{+,s',i+1} \rangle, \\
\Delta_{Q_m,-i'} &= \langle f_{-, (i+2)'}^\dagger f_{-, (i+1)'} \rangle, \\
\Delta_{Q_{i,+,-,\uparrow},i} &= \langle f_{+,\uparrow,i}^\dagger f_{-,i'} \rangle, \\
\Delta_{Q_{i,+,-,\downarrow},i} &= \langle f_{+,\downarrow,i}^\dagger f_{-,i'} \rangle.
\end{aligned} \tag{S39}$$

There are also conjugated parameters, which we omitted for brevity.

We first consider intra-valley $Q = 0$ channels. There are six charge order parameters:

$$\Gamma(Q = 0)^c = \left(\Delta_{Pom,+1}^c \Delta_{Pom,+2}^c \Delta_{Pom,+3}^c \Delta_{Pom,-,1'} \Delta_{Pom,-,2'} \Delta_{Pom,-,3'} \right).$$

As usual, we assume that bare order parameters are infinitesimally small and dress them by the interactions in the ladder approximation. We obtain

$$\Gamma(Q = 0)^c = \Gamma(Q = 0)^{c,(0)} + \Pi(0)\Lambda_{Q=0}^c \Gamma(Q = 0)^c, \quad (\text{S40})$$

where $\Pi(0)$ is the polarization operator, $\Gamma(Q = 0)^{c,(0)}$ is bare (infinitesimal) order parameter, and $\Gamma(Q = 0)^c$ is the dressed order parameter. The matrix $\Lambda_{Q=0}^c$ has the form

$$\Lambda_{Q=0}^c = \begin{pmatrix} -u & j-2u & j-2u & -u & -u & -u \\ j-2u & -u & j-2u & -u & -u & -u \\ j-2u & j-2u & -u & -u & -u & -u \\ -2u & -2u & -2u & 0 & j-u & j-u \\ -2u & -2u & -2u & j-u & 0 & j-u \\ -2u & -2u & -2u & j-u & j-u & 0 \end{pmatrix}. \quad (\text{S41})$$

The largest eigenvalue of this matrix is $\lambda_{Pom}^{c,s^\pm} = u+2j$ and the corresponding eigenvector is $(-\frac{1}{2}, -\frac{1}{2}, -\frac{1}{2}, 1, 1, 1)$. It describes s^\pm -wave charge Pomeranchuk order, which is symmetric with respect to 3 vH points from the same valley and changes sign between valleys. This order leads to valley polarization.

A $Q = 0$ spin order parameter can only be introduced for the spinfull valley, therefore

$$\Gamma(Q = 0)^s = \left(\Delta_{Pom,+1}^s \Delta_{Pom,+2}^s \Delta_{Pom,+3}^s \right)$$

with the coupling matrix

$$\Lambda_{Q=0}^s = \begin{pmatrix} u & j & j \\ j & u & j \\ j & j & u \end{pmatrix}. \quad (\text{S42})$$

The largest eigenvalue is again $u + 2j$. The corresponding eigenvector is $(1, 1, 1)$, i.e., this order is again s -wave with respect to three vH points from the same valley.

Now consider intra-valley density wave orders. In general, such an order can be with any momenta connecting vH points. Intra-valley density-wave orders are with momenta Q_m and inter-valley density-wave orders are with Q_l and Q_s (see Fig. S4).

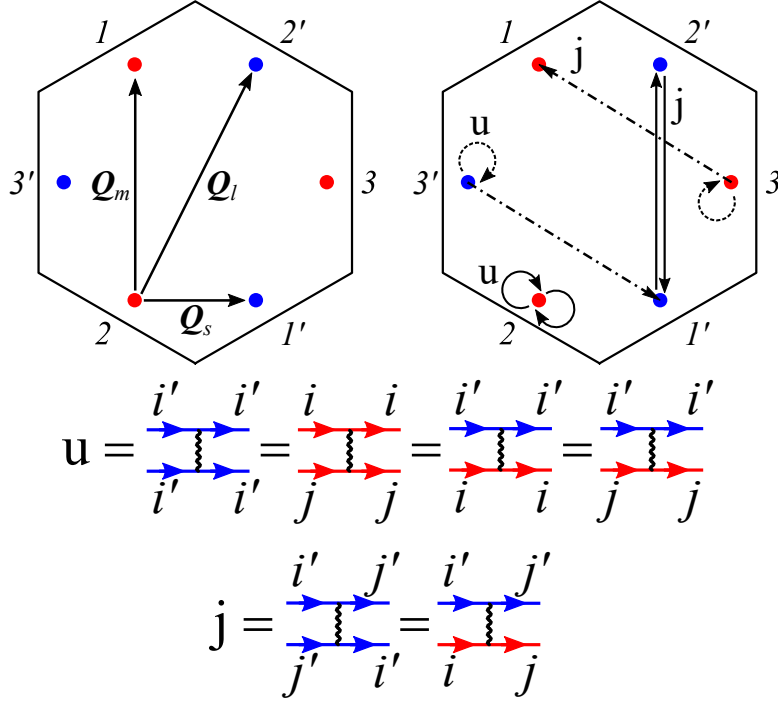


FIG. S4. Left: The sketch of a 6-patch model. Circles indicate the location of patches and color indicates valley composition. We assume that the blue valley is “spinless”. Vectors \mathbf{Q}_s , \mathbf{Q}_m , \mathbf{Q}_l connect patches in momentum space. Right: sketch of interactions between patch fermions. The couplings are shown below.

We begin with intra-valley orders. As for $Q = 0$, the order in the spin channel can be only introduced for the spinfull valley $+$. The corresponding order parameters are

$$\Gamma(Q_m)^s = (\Delta_{Q_m,+1}^s \Delta_{Q_m,+2}^s \Delta_{Q_m,+3}^s)$$

and the coupling matrix is

$$\Lambda_{Q_m}^s = u \mathbb{1}_{3 \times 3} \quad (\text{S43})$$

with three eigenvalues equal to u . The charge channel is more interesting. Here

$$\Gamma(Q_m)^c = (\Delta_{Q_m,+1}^c \Delta_{Q_m,+2}^c \Delta_{Q_m,+3}^c \bar{\Delta}_{Q_m,-,1'} \bar{\Delta}_{Q_m,-,2'} \bar{\Delta}_{Q_m,-,3'}),$$

where $\bar{\Delta}$ is a conjugate of Δ . The matrix of the couplings is

$$\Lambda_{Q_m}^c = \begin{pmatrix} u-2j & 0 & 0 & -j & 0 & 0 \\ 0 & u-2j & 0 & 0 & -j & 0 \\ 0 & 0 & u-2j & 0 & 0 & -j \\ -2j & 0 & 0 & u-j & 0 & 0 \\ 0 & -2j & 0 & 0 & u-j & 0 \\ 0 & 0 & -2j & 0 & 0 & u-j \end{pmatrix}. \quad (\text{S44})$$

The two eigenvalues of this matrix are u and $u-3j$.

Now we proceed to inter-valley orders. Note, that for inter-valley orders the spin/charge dichotomy does not work anymore. Consider first the orders with momentum Q_l . The order parameters are

$$\Gamma(Q_l) = (\Delta_{Q_l,+-,\uparrow,1} \Delta_{Q_l,+-,\uparrow,2} \Delta_{Q_l,+-,\uparrow,3} \Delta_{Q_l,+-,\downarrow,1} \Delta_{Q_l,+-,\downarrow,2} \Delta_{Q_l,+-,\downarrow,3}). \quad (\text{S45})$$

The coupling matrix is diagonal

$$\Lambda_{Q_l}^s = u\mathbb{1}_{6 \times 6} \quad (\text{S46})$$

and has identical eigenvalues u .

We now consider inter-valley orders with momentum Q_s . The corresponding order parameters are

$$\Gamma(Q_s) = (\Delta_{Q_s,+-,\uparrow,1} \Delta_{Q_s,+-,\uparrow,2} \Delta_{Q_s,+-,\uparrow,3} \Delta_{Q_s,+-,\uparrow,1'} \Delta_{Q_s,+-,\uparrow,2'} \Delta_{Q_s,+-,\uparrow,3'}). \quad (\text{S47})$$

The coupling matrix is

$$\Lambda_{Q_s} = \begin{pmatrix} u & 0 & 0 & j & 0 & 0 \\ 0 & u & 0 & 0 & j & 0 \\ 0 & 0 & u & 0 & 0 & j \\ j & 0 & 0 & u & 0 & 0 \\ 0 & j & 0 & 0 & u & 0 \\ 0 & 0 & j & 0 & 0 & u \end{pmatrix}. \quad (\text{S48})$$

The leading eigenvalue here is $u+j$. It again corresponds to s -wave order, symmetric with respect to three vH points from the same valley (or, equivalently, symmetric with respect to three possible Q_s between neighboring vH points from different valleys). Evaluating the products of the eigenvalues and

the polarizations to obtain dimensionless couplings and comparing different channels, we find that s -wave $Q = 0$ channel and s -wave Q_s channel are almost degenerate. This is the same type of degeneracy as in the model with spinfull fermions [28].

The outcome of this analysis is that there are 8 almost degenerate order parameters: one scalar intra-valley charge $Q = 0$ order parameter, one 3-component intra-valley $Q = 0$ vector spin order parameter, and four inter-valley order parameters with momenta Q_s , which one can treat as 4 scalars. These 8 order parameters form an adjoint representation of SU(3).

The matrix Green's function, symmetric with respect to 3 vH points from the same valley, is a 3×3 matrix in band space. The Green's function of free fermions is diagonal and isotropic:

$$\hat{G}_0 = \begin{pmatrix} G & 0 & 0 \\ 0 & G & 0 \\ 0 & 0 & G \end{pmatrix}, \quad (\text{S49})$$

where $G^{-1} = i\omega_m - \xi_k$ with Matsubara frequency ω_m and fermion dispersion ξ_k . We associate the bottom component with the spinless valley. Once the order sets in, the Green's function gets modified. It is convenient to introduce the valley polarization order parameter ϕ via

$$\Delta_{Pom,+}^c = \frac{1}{\sqrt{3}}\phi, \quad \Delta_{Pom,-}^c = -\frac{2}{\sqrt{3}}\phi, \quad (\text{S50})$$

and introduce inter-valley order parameters $S_{A1}, S_{A2}, S_{B1}, S_{B2}$ related to the magnitudes of inter-valley order parameters (identical for 3 directions of vectors Q_s) $\Delta_{Q_s,+-,\uparrow}, \Delta_{Q_s,+-,\downarrow}$ and their conjugated $\bar{\Delta}_{Q_s,+-,\uparrow}$ and $\bar{\Delta}_{Q_s,+-,\downarrow}$ via

$$\begin{aligned} S_{A2} - iS_{B2} &= \Delta_{Q_s,+-,\uparrow}, & S_{A1} - iS_{B1} &= \Delta_{Q_s,+-,\downarrow}, \\ S_{A2} + iS_{B2} &= \bar{\Delta}_{Q_s,+-,\uparrow}, & S_{A1} + iS_{B1} &= \bar{\Delta}_{Q_s,+-,\downarrow}, \end{aligned} \quad (\text{S51})$$

We label the three-component vector spin intra-valley order parameter $\Delta_{Pom,+}^s$ as just \mathbf{S} .

In matrix notations we then have $\hat{G} = \hat{G}_0 + \hat{\phi} + \hat{S} + \hat{S}_{AB}$, where

$$\begin{aligned}\hat{\phi} &= \frac{1}{\sqrt{3}} \begin{pmatrix} \phi & 0 & 0 \\ 0 & \phi & 0 \\ 0 & 0 & -2\phi \end{pmatrix}, \\ \hat{S} &= \begin{pmatrix} S_z & S_x - iS_y & 0 \\ S_x + iS_y & -S_z & 0 \\ 0 & 0 & 0 \end{pmatrix}, \\ \hat{S}_{AB} &= \begin{pmatrix} 0 & 0 & S_{A2} - iS_{B2} \\ 0 & 0 & S_{A1} - iS_{B1} \\ S_{A2} + iS_{B2} & S_{A1} + iS_{B1} & 0 \end{pmatrix}.\end{aligned}\tag{S52}$$

Expressed via the standard form of Gell-Mann matrices, $\hat{\phi}$ corresponds to matrix T^8 , \hat{S} corresponds to T^1, T^2, T^3 , and \hat{S}_{AB} corresponds to T^4, T^5, T^6, T^7 , where T^i with $i = 1 \dots 8$ are the eight generators of the group SU(3).

SUPPLEMENTARY DISCUSSION VII: THE GROUND STATE OF THE SU(3) MODEL IN TERMS OF FERMIONIC BILINEARS

The ordered state in the SU(3) model can be straightforwardly expressed via fermionic bilinears. For simplicity, we present the result for the case when inter-valley components S_{A1}, S_{A2} and S_{B1}, S_{B2} are absent and the order is specified by ϕ and \mathbf{S} . The same free energy as in (S35), expressed in terms of ϕ and \mathbf{S} is

$$F = \alpha(\phi^2 + \mathbf{S} \cdot \mathbf{S}) + \frac{2\gamma}{\sqrt{3}}\phi \left(\mathbf{S} \cdot \mathbf{S} - \frac{\phi^2}{3} \right) + \frac{\beta}{2}(\phi^2 + \mathbf{S} \cdot \mathbf{S})^2\tag{S53}$$

We introduce a standard parameterization for magnitudes of order parameters: $|\mathbf{S}| = r \cos \theta$, $\phi = r \sin \theta$ and rewrite the free energy in the form

$$F = \alpha r^2 + \frac{2\gamma}{3\sqrt{3}}r^3 \sin 3\theta + \frac{\beta}{2}r^4.\tag{S54}$$

The ground state is reached when $\sin 3\theta = -1$, i.e., for $\theta = \frac{\pi}{2}, \frac{7\pi}{6}, \frac{11\pi}{6}$. The ordered states, which we earlier specified by $\hat{\Phi} = (\lambda, \lambda, -2\lambda)$ (up to permutations) with λ given by Eq. (S33), are expressed in

terms of ϕ and S as

$$\begin{aligned}
\phi &= r, |S| = 0, \\
\phi &= -\frac{r}{2}, |S| = -\frac{r\sqrt{3}}{2}, \\
\phi &= -\frac{r}{2}, |S| = \frac{r\sqrt{3}}{2}.
\end{aligned} \tag{S55}$$

The first state is a pure valley order, for which the two-fold degeneracy stems from the unbroken spin degeneracy of the spinfull valley. The other two states correspond to mixed spin-valley order. There, the degenerate levels necessarily belong to different valleys, however, spin directions remain degenerate.

SUPPLEMENTARY DISCUSSION VIII: ANOTHER SCENARIO FOR THE CASCADE OF TRANSITIONS

Here we discuss another scenario for the cascade, in which the component of the van Hove peak that crosses the Fermi level, no longer contributes to particle-hole order. This scenario is qualitatively similar to the one put forward in Ref. [15], in which one of the bands gets fully filled (fully depleted) at each transition from the cascade and after that does not contribute to particle-hole order, and to the one in Ref. [14], in which a flat band gets severely broadened after crossing the Fermi level. We do not assume full filling/full depletion or strong broadening, but still exercise here the idea that one of the bands effectively disappears after each transition, and the symmetry of the Landau free energy progressively reduces from SU(4) to SU(3) and then to SU(2). In this scenario the pattern of symmetry changes at the transitions from the cascade is

$$\begin{aligned}
n \approx 1 &: \text{SU}(4) \rightarrow \text{SU}(3) \times \text{U}(1) \\
n \approx 2 &: \text{SU}(3) \rightarrow \text{SU}(2) \times \text{U}(1) \\
n \approx 3 &: \text{SU}(2) \rightarrow \text{U}(1).
\end{aligned} \tag{S56}$$

and the number of relevant bands that contribute to particle-hole orders changes from 4 to 3 at $|n| \approx 1$, from 3 to 2 at $|n| \approx 2$, and from 2 to 1 at $|n| \approx 3$.

The first transition and the manifold of the ordered states is exactly the same as in the SU(4) model from the main text, and the splitting of the vH peak is 3-1, with one component crossing the Fermi level. At the second transition, one component of 3-fold degenerate vH peak crosses the Fermi level. The manifold of the ordered states is the same as in the 2-2 phase of the SU(4) model.

For the last transition, the relevant model contains either two spinless fermions from different valleys or one valley with both spin projections. In either case the system obeys $SU(2)$ symmetry: in valley space in the former and in spin space in the latter. For the valley $SU(2)$ case the only particle-hole order parameter is charge valley polarization. Interaction for this order parameter is attractive, and gives rise to an instability that moves one vH peak component through the Fermi level and splits the doubly degenerate vH peak into 1-1. For the spin $SU(2)$ case the only instability is the standard Stoner-like ferromagnetism that leads to the splitting of two levels. Finally, as $|n|$ comes close to 4, the last vH peak component moves through the Fermi level.

Note that the first two transitions, near $|n| = 1$ and $|n| = 2$, are first order, the one near $|n| = 3$ is second order, and the last crossing near $|n| = 4$ is continuous in our present description, but may actually also involve a phase transition, as we argue in the next subsection.

Within this scenario, one can naturally explain the emergence of insulating states at integer fillings, but it is a priori unclear how the peak components which are assumed to be at different energies as they cross the Fermi level at different n , recombine back into a 4-fold degenerate strong vH peak once the order disappears at $|n| \lesssim 4$.

SUPPLEMENTARY DISCUSSION IX: INSTABILITY OF SPINLESS FERMIONS FROM A SINGLE VALLEY

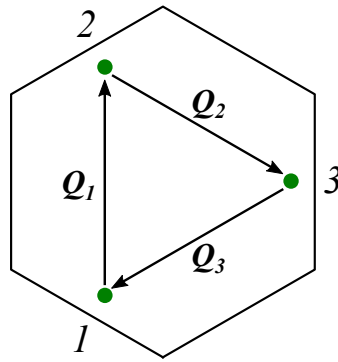


FIG. S5. The sketch of a patch model for a band with only one occupied valley. Green circles indicate the location of van Hove points. Three vectors indicate the directions of momentum transfer between each pair of patches. This is the momentum transfer of the density wave.

Above we considered vH points that are related by C_3 lattice rotational symmetry and assumed that magnitudes of order parameter are identical on every patch. Here we relax this assumption and check if other particle-hole orders are possible. This issue is most relevant for the case of spinless fermions near 3 vH points in only one valley i.e., the case near $|n| \lesssim 4$ when only one fermion species from a single valley remains.

We label the fermions from the three vH points as f_i , $i = 1, 2, 3$, see Fig. S5. Because fermions are spinless, only charge orders are possible. There are two potential orders: the one with $Q = 0$ and the one with Q between van Hove points. Each order parameter has three components. The order parameters are

$$\begin{aligned}\Delta_{Pom,i} &= \langle f_i^\dagger f_i \rangle, \\ \Delta_{Q_i} &= \langle f_{i+1}^\dagger f_i \rangle.\end{aligned}\tag{S57}$$

Like in Supplementary Discussion VI we consider density-density and exchange interactions (u and j terms, respectively). In the ladder approximation the two order parameters do not couple and can be considered independent of each other. For the three $Q = 0$ order parameters the coupling matrix is

$$\Lambda_{Q=0} = \begin{pmatrix} 0 & j-u & j-u \\ j-u & 0 & j-u \\ j-u & j-u & 0 \end{pmatrix}\tag{S58}$$

There are three eigenvalues: $\lambda^s = 2(j-u)$, which corresponds to an s -wave order parameter with eigenvector $(1, 1, 1)$, and two-fold degenerate $\lambda^d = u-j$, with d -wave eigenvectors $(-1, 0, 1)$ and $(1/2, -1, 1/2)$. For $u > j$, as expected on general grounds, λ^d is positive (attractive) and λ^s is negative (repulsive). If the s -wave $Q = 0$ order parameter is imposed, the vH peak crosses the Fermi level without inducing a particle-hole order.

For finite Q orders, the coupling matrix is

$$\Lambda_Q = \begin{pmatrix} u-j & 0 & 0 \\ 0 & u-j & 0 \\ 0 & 0 & u-j \end{pmatrix}.\tag{S59}$$

We see that the eigenfunctions for all three combinations of Δ_{Q_i} (one is s -wave and two are d -wave) are identical and the same as for the d -wave $Q = 0$ order parameter. The polarization operator for $Q = 0$ is slightly larger than the one with finite Q (Ref. [28]). Hence d -wave $Q = 0$ order is the most

likely one. Such an order splits the energies of the three vH peaks. So far, no clear evidence for such order has been reported, see however, Ref. 60. One option may be that such order oscillates between the two d -wave components at short spatial scales, and on average all three vH peaks move identically, like if there was no particle-hole order.

SUPPLEMENTARY DISCUSSION X: CASCADE OF TRANSITIONS IN BERNAL BILAYER GRAPHENE AND IN RHOMBOHEDRAL TRILAYER GRAPHENE IN THE 2-PATCH MODEL

In this section we discuss the extension of our analysis to cases of Bernal Bilayer Graphene (BBG) and Rhombohedral Trilayer Graphene (RTG). Band structure and Fermi surfaces of both systems are extremely similar, therefore, we consider them under one umbrella in this manuscript.

Our VH scenario can be successfully applied to the problem of cascade of electronic transitions in Bernal bilayer (BBG) and rhombohedral trilayer graphene (RTG). Here we consider a minimal 2-patch model to describe the cascade in BBG and RTG. We discuss an extension to a 6-patch model in the next section.

The two-patch model describes fermions in the vicinity of K and K' points in the hexagonal Brillouin zone (BZ). This model is based on realistic tight-binding models for BBG [47–49] and RTG [50, 51] in the presence of a displacement field, which opens a gap between the conduction and valence bands [46]. We assume that the chemical potential is near vH doping close to charge neutrality. In this case, the Fermi surface of both BBG and RTG either has the shape of three touching small Fermi pockets at K and K' points (6 Van Hove singularities total), or has one higher-order vH singularity (HOVHS) per valley located exactly at K (K'), see Fig. S6. Because three vH points per valley are located very close to each other in the BZ, we assume that the couplings between them are the same and that the small difference in wave vectors connecting vH points within a valley can be neglected, i.e. possible wave vector transfers between vH points are approximately zero or $K - K'$. In this case, we can consider one patch per valley K, K' that describes spin-degenerate fermionic states with dispersion $\varepsilon \simeq k_x^2 - k_y^2$.

We model the interaction via equal intra- and inter-patch density-density couplings and neglect valley mixing terms. This last assumption has been widely used for TBG. Its validity for non-twisted BBG and RTG in the absence of a displacement field is not justified [61, 62], but we conjecture, following [63] that in the presence of a sizable displacement field exchange processes between the two valleys are small.

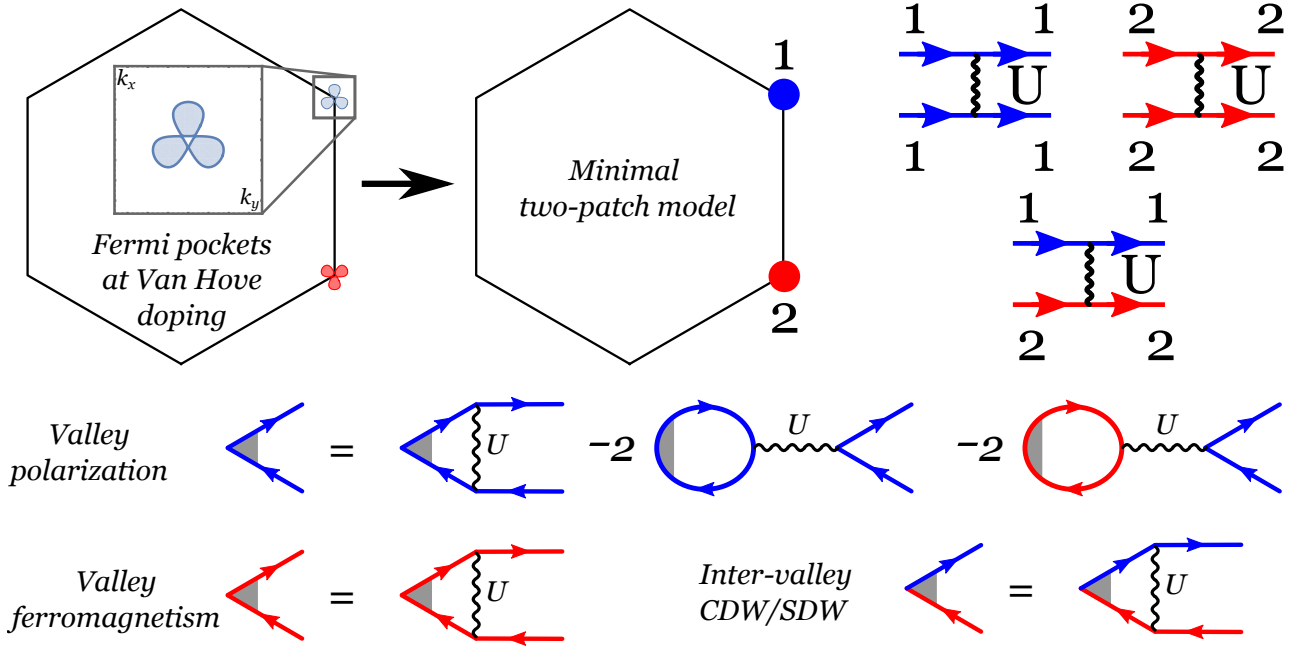


FIG. S6. Top: sketch of Fermi surface at vH doping in Bernal bilayer graphene and rhombohedral trilayer graphene in a displacement field. It can be approximated by a 2-patch model with density-density interactions between patches 1 and 2. Bottom: the system of coupled equations for particle-hole instabilities in the 2-patch model.

The interaction Hamiltonian with density-density couplings reads

$$H_{int} = \sum_{i,j=1,2;\sigma,\sigma'=\uparrow,\downarrow} (U f_{i\sigma}^\dagger f_{i\sigma} f_{j\sigma'}^\dagger f_{j\sigma'}), \quad (\text{S60})$$

where i is the patch (valley) index, and σ, σ' are spin indices (see Fig. S6). To study potential instabilities of the Fermi liquid within the RPA approach, we write down the system of coupled equations for test vertices in spin and charge channels for the two patches. Its diagrammatic representation is shown in Fig. S6. In our 2-patch approximation, the polarization bubble $\Pi(0) = \Pi(K - K')$ so that $Q = 0$ channels and density waves with $Q = K - K'$ are exactly degenerate. Moreover, those instabilities are described by exactly the same 15 fields ϕ_j and the same SU(4)-symmetric Landau free energy functional as in the case of TBG. This, in turn, yields the same physics of the cascade and the same resulting ground states as in the case of TBG.

SUPPLEMENTARY DISCUSSION XI: CASCADE OF TRANSITIONS IN BERNAL BILAYER GRAPHENE AND IN RHOMBOHEDRAL TRILAYER GRAPHENE IN THE 6-PATCH MODEL

As a next step, we distinguish the states near the six vH points and model each of them via a hyperbolic dispersion relation valid in a patch around the vH point of the form $\varepsilon \simeq k_x^2 - k_y^2$ and its rotations by $2\pi/3$, respectively. The structure of patch model in momentum space is shown in Fig. S7. For the interaction, we can distinguish five different magnitudes of momentum-transfer vectors. Some of them (Q_Δ) connect patches within a valley, the other $Q_1, Q_{1'}, Q_2, Q_3$ represent momentum transfers between different valleys. Allowing for density-density couplings u and exchange couplings j between the different patches and neglecting valley mixing, we obtain the interaction Hamiltonian

$$\begin{aligned}
 H_{int} = & \sum_{i,m=1,2,3;s,s'=\uparrow,\downarrow} \left[u f_{i,s,+}^\dagger f_{i,s,+} f_{m,s',+}^\dagger f_{m,s',+} + \right. \\
 & + u f_{i',s,-}^\dagger f_{i',s,-} f_{m',s',-}^\dagger f_{m',s',-} + u f_{i,s,+}^\dagger f_{i,s,+} f_{m',s',-}^\dagger f_{m',s',-} \\
 & + j f_{i,s,+}^\dagger f_{i+1,s,+} f_{i+1,s',+}^\dagger f_{i+1,s',+} + j f_{i',s,-}^\dagger f_{(i+1)',s,-} f_{(i+1)',s',-}^\dagger f_{(i+1)',s',-} \\
 & \left. + j f_{i,s,+}^\dagger f_{i+1,s,+} f_{i',s',-}^\dagger f_{(i+1)',s',-} \right], \tag{S61}
 \end{aligned}$$

where i, m are patch indices, $+, -$ label valley, and s, s' are spin indices. The relevant scattering processes are shown in Fig. S8.

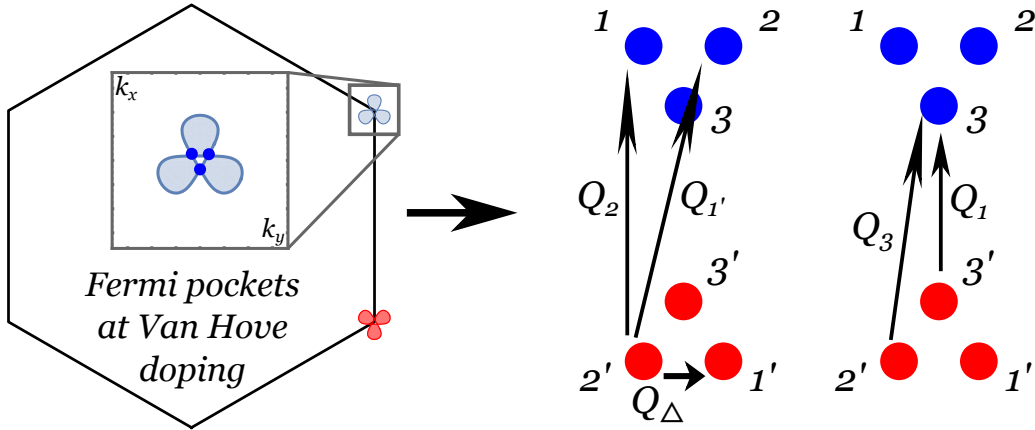


FIG. S7. Sketch of the 6-patch model with one patch per vH point and different wave vectors connecting them. Blue circles indicate positions of vH points.

We classify the possible order parameters by the values of momentum transfer, valley composition, and if the instability is in charge or spin channel. In total, there are $144-1=143$ possible components

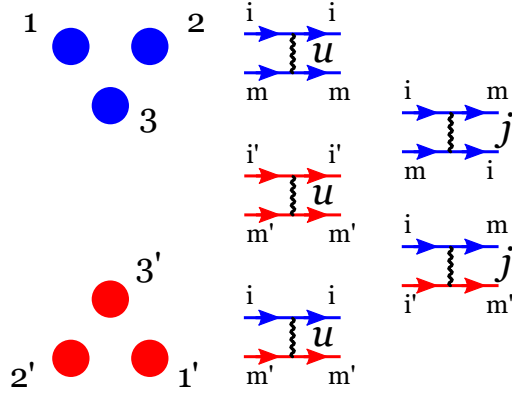


FIG. S8. Density-density and exchange interactions between patch fermions, governed by the Hamiltonian (S61).

of particle-hole order parameters that can be cast into a scalar (for charge order) or vector (for spin order) form like in the patch model treatment of twisted bilayer graphene [28]. All these possible order parameters that involve fermions in the vicinity of vH points are

$$\begin{aligned}
\Delta(0)_{i,+}^c &= \langle f_{s,i,+}^\dagger \delta_{ss'} f_{s',i,+} \rangle, & \Delta(0)_{i,+}^s &= \langle f_{s,i,+}^\dagger \sigma_{ss'} f_{s',i,+} \rangle, \\
\Delta(0)_{i',-}^c &= \langle f_{s,i',-}^\dagger \delta_{ss'} f_{s',i',-} \rangle, & \Delta(0)_{i',-}^s &= \langle f_{s,i',-}^\dagger \sigma_{ss'} f_{s',i',-} \rangle, \\
\Delta(\mathcal{Q}_\Delta)_{i,+}^c &= \langle f_{s,i+2,+}^\dagger \delta_{ss'} f_{s',i+1,+} \rangle, \\
\Delta(\mathcal{Q}_\Delta)_{i,+}^s &= \langle f_{s,i+2,+}^\dagger \sigma_{ss'} f_{s',i+1,+} \rangle, \\
\Delta(\mathcal{Q}_\Delta)_{i',-}^c &= \langle f_{s,i'+2,-}^\dagger \delta_{ss'} f_{s',i'+1,-} \rangle, \\
\Delta(\mathcal{Q}_\Delta)_{i',-}^s &= \langle f_{s,i'+2,-}^\dagger \sigma_{ss'} f_{s',i'+1,-} \rangle, \\
\Delta(\mathcal{Q}_1)^c &= \langle f_{s,3,+}^\dagger \delta_{ss'} f_{s',3,-} \rangle, & \Delta(\mathcal{Q}_1)^s &= \langle f_{s,3,+}^\dagger \sigma_{ss'} f_{s',3,-} \rangle, \\
\Delta(\mathcal{Q}_{1'})_{i=1,2}^c &= \langle f_{s,i,+}^\dagger \delta_{ss'} f_{s',i',-} \rangle, & \Delta(\mathcal{Q}_{1'})_{i=1,2}^s &= \langle f_{s,i,+}^\dagger \sigma_{ss'} f_{s',i',-} \rangle, \\
\Delta(\mathcal{Q}_2)_1^c &= \langle f_{s,1,+}^\dagger \delta_{ss'} f_{s',2,-} \rangle, & \Delta(\mathcal{Q}_2)_1^s &= \langle f_{s,1,+}^\dagger \sigma_{ss'} f_{s',2,-} \rangle, \\
\Delta(\mathcal{Q}_2)_2^c &= \langle f_{s,2,+}^\dagger \delta_{ss'} f_{s',1,-} \rangle, & \Delta(\mathcal{Q}_2)_2^s &= \langle f_{s,2,+}^\dagger \sigma_{ss'} f_{s',1,-} \rangle, \\
\Delta(\mathcal{Q}_3)_1^c &= \langle f_{s,3,+}^\dagger \delta_{ss'} f_{s',1,-} \rangle, & \Delta(\mathcal{Q}_3)_1^s &= \langle f_{s,3,+}^\dagger \sigma_{ss'} f_{s',1,-} \rangle, \\
\Delta(\mathcal{Q}_3)_2^c &= \langle f_{s,3,+}^\dagger \delta_{ss'} f_{s',2,-} \rangle, & \Delta(\mathcal{Q}_3)_2^s &= \langle f_{s,3,+}^\dagger \sigma_{ss'} f_{s',2,-} \rangle, \\
\Delta(\mathcal{Q}_3)_{1'}^c &= \langle f_{s,1,+}^\dagger \delta_{ss'} f_{s',3,-} \rangle, & \Delta(\mathcal{Q}_3)_{1'}^s &= \langle f_{s,1,+}^\dagger \sigma_{ss'} f_{s',3,-} \rangle, \\
\Delta(\mathcal{Q}_3)_{2'}^c &= \langle f_{s,2,+}^\dagger \delta_{ss'} f_{s',3,-} \rangle, & \Delta(\mathcal{Q}_3)_{2'}^s &= \langle f_{s,2,+}^\dagger \sigma_{ss'} f_{s',3,-} \rangle,
\end{aligned} \tag{S62}$$

where $+$, $-$ labels the two valleys, s , s' labels spin, $i = 1, 2, 3$ are the patch numbers unless specified

otherwise, and σ is the vector of Pauli matrices. For brevity, we did not list complex conjugates of the order parameters.

To determine possible Fermi liquid instabilities, we introduce infinitesimally small bare order parameters $\Gamma(Q)_{inter/intra}^{c,s,(0)}$ and consider their dressing by interactions in the ladder (RPA) approximation. In this approximation the dressed order parameter is given by

$$\Gamma(Q)_{inter/intra}^{c,s} = \Gamma(Q)_{inter/intra}^{c,s,(0)} + \Pi(Q)\Lambda(Q)_{inter/intra}^{c,s}\Gamma(Q)_{inter/intra}^{c,s},$$

where the matrix $\Lambda(Q)_{inter/intra}^{c,s}$ contains the couplings between test vertices. We start by considering the $Q = 0$ channels. For the $Q = 0$ charge channel

$$\Gamma(0)^c = (\Delta(0)_{1,+}^c, \Delta(0)_{2,+}^c, \Delta(0)_{3,+}^c, \Delta(0)_{1',-}^c, \Delta(0)_{2',-}^c, \Delta(0)_{3',-}^c)$$

and the coupling matrix reads

$$\Lambda(0)^c = \begin{pmatrix} -u & j-2u & j-2u & -2u & -2u & -2u \\ j-2u & -u & j-2u & -2u & -2u & -2u \\ j-2u & j-2u & -u & -2u & -2u & -2u \\ -2u & -2u & -2u & -u & j-2u & j-2u \\ -2u & -2u & -2u & j-2u & -u & j-2u \\ -2u & -2u & -2u & j-2u & j-2u & -u \end{pmatrix}. \quad (\text{S63})$$

Its largest eigenvalue $u+2j$ corresponds to a valley charge order with an s^\pm form factor $(1, 1, 1, -1, -1, -1)$.

The test vertex for a $Q = 0$ instability in the spin channel is

$$\Gamma(0)^s = (\Delta(0)_{1,+}^s, \Delta(0)_{2,+}^s, \Delta(0)_{3,+}^s, \Delta(0)_{1',-}^s, \Delta(0)_{2',-}^s, \Delta(0)_{3',-}^s)$$

and the coupling matrix is

$$\Lambda(0)^s = \begin{pmatrix} u & j & j & 0 & 0 & 0 \\ j & u & j & 0 & 0 & 0 \\ j & j & u & 0 & 0 & 0 \\ 0 & 0 & 0 & u & j & j \\ 0 & 0 & 0 & j & u & j \\ 0 & 0 & 0 & j & j & u \end{pmatrix}. \quad (\text{S64})$$

The largest eigenvalue is again $u+2j$. It corresponds to two eigenvectors $(1, 1, 1, 0, 0, 0)$ and $(0, 0, 0, 1, 1, 1)$ that describe two independent valley ferromagnets with arbitrary orientation of magnetization vectors. Thus, the instabilities towards valley charge order and valley ferromagnetism are degenerate.

In contrast to the 2-patch model, there are also intra-valley spin (SDW) and charge (CDW) density waves with momentum transfer \mathbf{Q}_Δ in the 6-patch model. The test vertex for the CDW reads

$$\Gamma(\mathbf{Q}_\Delta)^c = \left(\Delta(\mathbf{Q}_\Delta)_{1,+}^c, \Delta(\mathbf{Q}_\Delta)_{2,+}^c, \Delta(\mathbf{Q}_\Delta)_{3,+}^c, \Delta(\mathbf{Q}_\Delta)_{1',-}^c, \Delta(\mathbf{Q}_\Delta)_{2',-}^c, \Delta(\mathbf{Q}_\Delta)_{3',-}^c \right) \quad (\text{S65})$$

and the coupling matrix is given by

$$\Lambda(\mathbf{Q}_\Delta)^c = \begin{pmatrix} u-2j & 0 & 0 & -2j & 0 & 0 \\ 0 & u-2j & 0 & 0 & -2j & 0 \\ 0 & 0 & u-2j & 0 & 0 & -2j \\ -2j & 0 & 0 & u-2j & 0 & 0 \\ 0 & -2j & 0 & 0 & u-2j & 0 \\ 0 & 0 & -2j & 0 & 0 & u-2j \end{pmatrix}. \quad (\text{S66})$$

The maximal eigenvalues of this coupling matrix is u . For intra-valley SDW with

$$\Gamma(\mathbf{Q}_\Delta)^s = \left(\Delta(\mathbf{Q}_\Delta)_{1,+}^s, \Delta(\mathbf{Q}_\Delta)_{2,+}^s, \Delta(\mathbf{Q}_\Delta)_{3,+}^s, \Delta(\mathbf{Q}_\Delta)_{1',-}^s, \Delta(\mathbf{Q}_\Delta)_{2',-}^s, \Delta(\mathbf{Q}_\Delta)_{3',-}^s \right) \quad (\text{S67})$$

the coupling matrix is diagonal

$$\Lambda(\mathbf{Q}_\Delta)^s = u\mathbb{1}_{6 \times 6},$$

where $\mathbb{1}_{6 \times 6}$ is a 6×6 diagonal matrix in patch space. Hence, for intra-valley channels, instabilities towards charge and spin density waves are degenerate within RPA.

We now move to inter-valley channels. The couplings in charge and spin inter-valley density wave channels are degenerate. The density-wave order parameter with momentum \mathbf{Q}_1 and $\Gamma(\mathbf{Q}_1)^{c,s} = \Delta(\mathbf{Q}_1)^{c,s}$ couples only to itself. Therefore, the only eigenvalue is u . For $\mathbf{Q}_{1'}$, $\Gamma(\mathbf{Q}_{1'})^{c,s} = \left(\Delta(\mathbf{Q}_{1'})_1^{c,s}, \Delta(\mathbf{Q}_{1'})_2^{c,s} \right)$ has two components and the coupling matrix is diagonal

$$\Lambda(\mathbf{Q}_{1'})^{c,s} = u\mathbb{1}_{2 \times 2}. \quad (\text{S68})$$

For the order parameter with momentum Q_2 , with

$$\Gamma(Q_2)^{c,s} = (\Delta(Q_2)_1^{c,s}, \Delta(Q_2)_2^{c,s}),$$

the coupling matrix reads

$$\Lambda(Q_2)^{c,s} = \begin{pmatrix} u & j \\ j & u \end{pmatrix} \quad (\text{S69})$$

and the largest eigenvalue is $u + j$. The coupling matrix for Q_3 with

$$\Gamma(Q_3)_1^{c,s} = (\Delta(Q_2)_1^{c,s}, \Delta(Q_2)_{1'}^{c,s})$$

and

$$\Gamma(Q_3)_2^{c,s} = (\Delta(Q_2)_2^{c,s}, \Delta(Q_2)_{2'}^{c,s})$$

is identical to $\Lambda(Q_2)^{c,s}$. Hence, it yields the same leading eigenvalue.

In order to find the leading instability we need to know the values of polarization operators. We find that the two largest polarization operators are $\Pi(0) > \Pi(Q_2)$ with nearly equal values. The other $\Pi(Q_{i \neq 2})$ are somewhat smaller in magnitude. Neglecting the other finite Q channels, we obtain that the leading instabilities are degenerate $Q = 0$ valley ferromagnetism and charge valley order, or degenerate inter-valley spin/charge density waves with momentum transfer of magnitude Q_2 . The instability towards $Q = 0$ orders occurs when

$$1 - \Pi(0)(u + 2j) = 0 \quad (\text{S70})$$

and for $Q = Q_2$ when

$$1 - \Pi(Q_2)(u + j) = 0. \quad (\text{S71})$$

For $j > 0$, as we assumed to hold, the leading instabilities are with $Q = 0$, i.e. two independent intra-valley ferromagnetic instabilities (every patch develops ferromagnetism independent from the other one) and a valley charge instability. This valley charge order results in a different population of the two valleys. For valley charge order the order parameter is of the form $\phi = \sum_{i=1}^3 \langle f_{s,i,+}^\dagger \delta_{ss'} f_{s',i,+} \rangle - \langle f_{s,i,-}^\dagger \delta_{ss'} f_{s',i,-} \rangle$ and for the two valley ferromagnets the order parameters are $\mathcal{S}_1 = \sum_{i=1}^3 \langle f_{s,i,+}^\dagger \sigma_{ss'} f_{s',i,+} \rangle$ and $\mathcal{S}_2 = \sum_{i=1}^3 \langle f_{s,i,-}^\dagger \sigma_{ss'} f_{s',i,-} \rangle$. Thus, the leading instabilities are described by the order parameter matrix $\hat{\Phi}_7$ from (S29). As we showed above, this leads to the same cascade of transitions as in the SU(4) symmetric case. We note that if $\Pi(Q_2)$ becomes larger than $\Pi(0)$ (and j remains small), spin and charge density waves with wave vector Q_2 are the leading instability. In this case, the symmetry between the three pockets around K, K' is broken together with threefold rotation symmetry.